Applied Ocean Research 117 (2021) 102963

Contents lists available at ScienceDirect

Applied Ocean Research

journal homepage: www.elsevier.com/locate/apor

An improved moving particle semi-implicit method for interfacial flows

Xiao Wen, Weiwen Zhao, Decheng Wan *

Computational Marine Hydrodynamics Lab (CMHL), School of Naval Architecture, Ocean and Civil Engineering, Shanghai Jiao Tong University, Shanghai 200240, China

ARTICLE INFO

Keywords:
MPS
Multiphase method
Interfacial flow
Rayleigh-taylor instability
Bubble rising
Dam-break flow
Internal solitary wave

ABSTRACT

In this paper, the improved moving particle semi-implicit (IMPS) method is further developed into a multiphase method by introducing various multiphase models. Then, the developed multiphase MPS method is applied to a variety of 2-D/3-D simulations of interfacial flows, including Rayleigh-Taylor instability, bubble rising, dam-break flow, and internal solitary waves. The fair agreements between the results of MPS and other reference results demonstrate that the present multiphase MPS method is stable and accurate enough to capture the interface with a large deformation in different flow problems. The phenomenon of air entrapment induced by the dam-break flow is well reproduced in the multiphase simulation and its influence on impact pressure is discussed in detail. The internal solitary waves with different amplitudes are numerically generated and the wave heights show a good agreement with experimental data even after a long-distance propagation, indicating that the numerical diffusion of the present multiphase MPS method is relatively low and the energy conservation can be ensured.

1. Introduction

In ocean engineering, there exist many interfacial flows phenomena, that is, flow fields with different fluids are separated by sharp interfaces, such as the bubbly flow (e.g., Chen et al., 2019; Abbaszadeh et al., 2020), interfacial wave (e.g., Grisouard et al., 2011; Zou et al., 2020), underwater explosion (e.g., Klaseboer et al., 2005; Wang et al., 2020), etc. Given the complexity and high cost of experimental research, Computational Fluid Dynamics (CFD) has gradually become an important numerical tool for interfacial flows, especially with the rapid development of computer technology in the last decades. In order to better reproduce the violent hydrodynamic phenomena appearing in the interfacial flows and capture the complex interfaces accurately, a variety of multiphase methods have been developed and applied (e.g., Ketabdari et al., 2008; Wan et al., 2010; Marsooli and Wu, 2014; Sampath and Zabaras, 2015; Lyu et al., 2017; Zhang et al., 2021c). However, most of multiphase methods are based on the mesh-based theory, such as Volume Of Fluid (VOF), Level Set (LS), Front Tracking (FT), etc., in which the discretization of fluid domain is implemented in the Eulerian mesh system. After a relatively long period of development, the theoretical basis of mesh-based methods has been quite mature and is widely followed by most of commercial software. However, complicated interface-capturing algorithms need to be carried out to trace the interfaces in the mesh-based method, which would bring additional calculation errors. Especially, when the interfacial flows become violent and cause the large deformation of phase interface, the accuracy of interface-capturing algorithms encounters great challenges.

In recent decades, the mesh-free method, also known as particle method, was proposed as the next generation of CFD method. Different from the mesh-based method, the fluid domain in the mesh-free method is discretized by a set of space particles, which carrys physical quantities, such as mass, velocity, pressure, etc., and can freely move in a Lagrangian coordinate system. According to the distribution of particles, the shape of free surface can be conveniently obtained without special interface-capturing algorithms. Therefore, the mesh-free method is suitable to simulate the violent flows with large deformations of free surface in ocean engineering, such as sloshing flow (Gotoh et al., 2014; Zhang et al., 2020, 2021b), dam-break flow (Crespo et al., 2008; Zhang and Wan, 2011), water entry problem (Cheng et al., 2020; Khayyer and Gotoh, 2016), wave-body interaction (Zhang and Wan, 2017; Rao and Wan, 2018; Di et al., 2021; Quartier et al., 2021), fluid-structure interaction (Gotoh et al., 2021; Zhang et al., 2021a), granular flow (Bhat and Pahar, 2021; Xie et al., 2021) and so on. Review on developments of mesh-free method can be further referred in Gotoh and Khayyer (2016, 2018), as well as recently by Luo et al. (2021). In addition, benefitting from the use of substantial derivative in governing equations, numerical

* Corresponding author.
E-mail address: dcwan@sjtu.edu.cn (D. Wan).

https://doi.org/10.1016/j.apor.2021.102963
Received 10 April 2021; Received in revised form 12 October 2021; Accepted 8 November 2021
Available online 17 November 2021

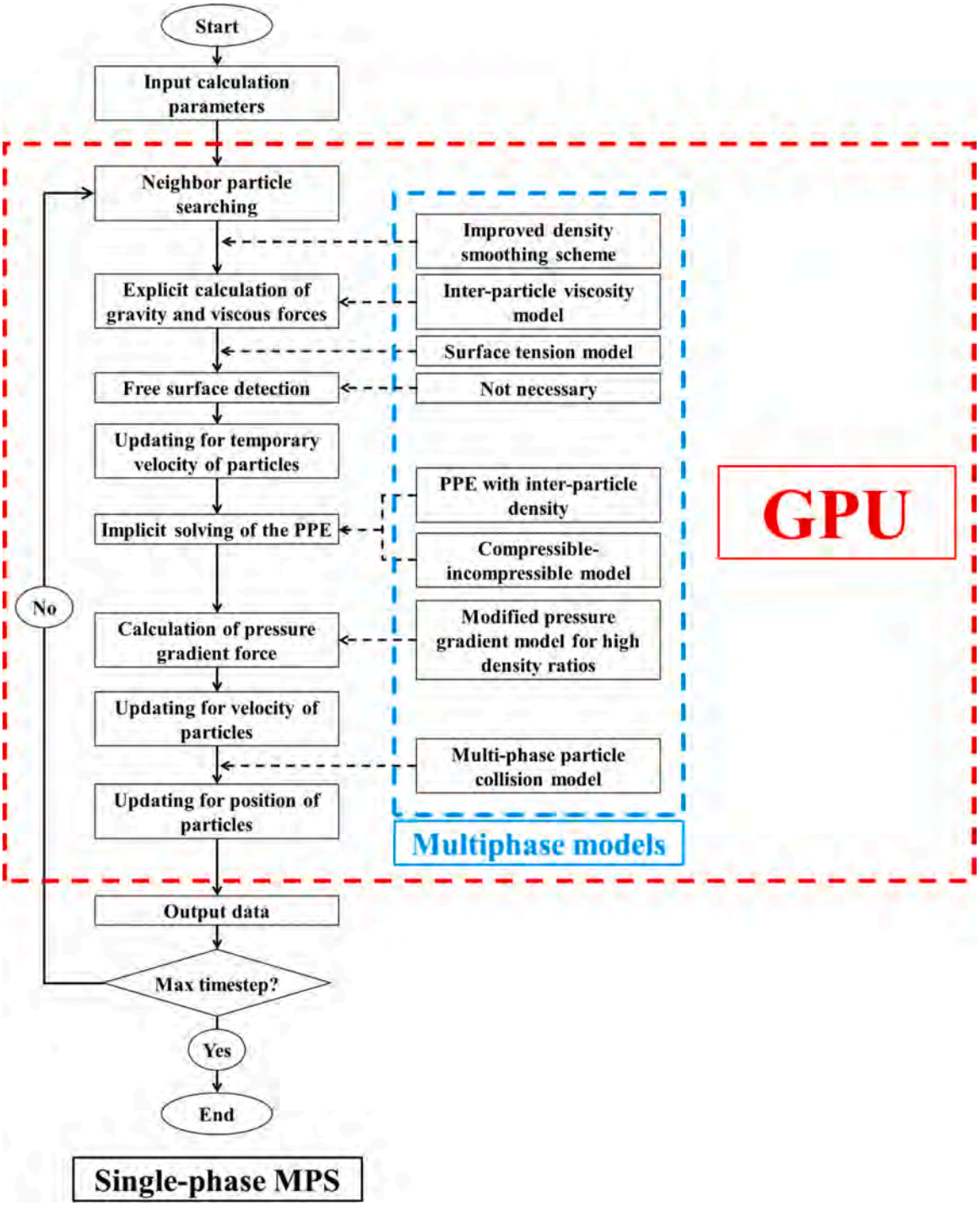

Fig. 1. Flowchart of multiphase MPS method with GPU acceleration technique.

diffusion induced by the discretization of convection term is eliminated in the mesh-free method.

There are two common mesh-free methods, including the smoothed particle hydrodynamics (SPH, Gingold and Monaghan, 1977; Lucy, 1977) method and the moving particle semi-implicit (MPS, Koshizuka and Oka, 1996) method. The basic principles of these two methods are exactly the same, such as the Lagrangian description of flow field, discretization of fluid domain by particles, and the particle interaction weighted by kernel function. The main difference is that the SPH method adopts an explicit algorithm based on the Equation of State (EoS), while a semi-implicit algorithm is employed in MPS method and the pressure field is calculated by solving the Poisson Pressure Equation (PPE). Thus, the MPS method fully guarantees the incompressible of the fluid, while the fluid simulated by SPH is allowed a slight compressibility. However, the above difference is becoming less obvious with the developments of incompressible smoothed particle hydrodynamics (ISPH, Shao and Lo, 2003; Lee et al., 2008; Gotoh et al., 2014) method and weakly compressible moving particle semi-implicit (WC-MPS, Jandaghian and Shakibaeinia, 2020; Shakibaeinia and Jin, 2010; Altomare et al., 2021) method. Later after, the difference between MPS and SPH mainly corresponds to their incorporated differential operator models, which is caused by the different considerations and derivations of inter-particle interaction.

When initially proposed by Koshizuka and Oka (1996), the MPS

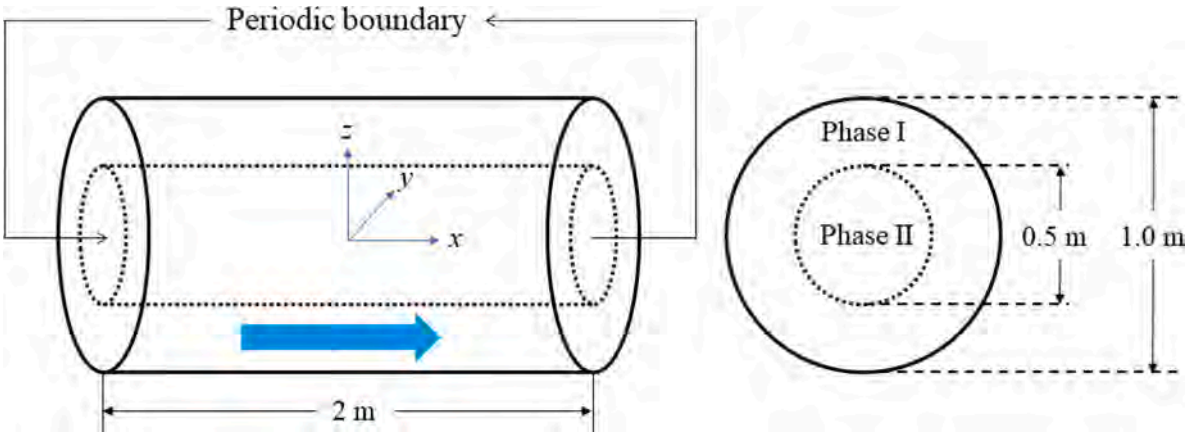

Fig. 2. Schematic diagram of multiphase Poiseuille flow in a 3-D circular tube.

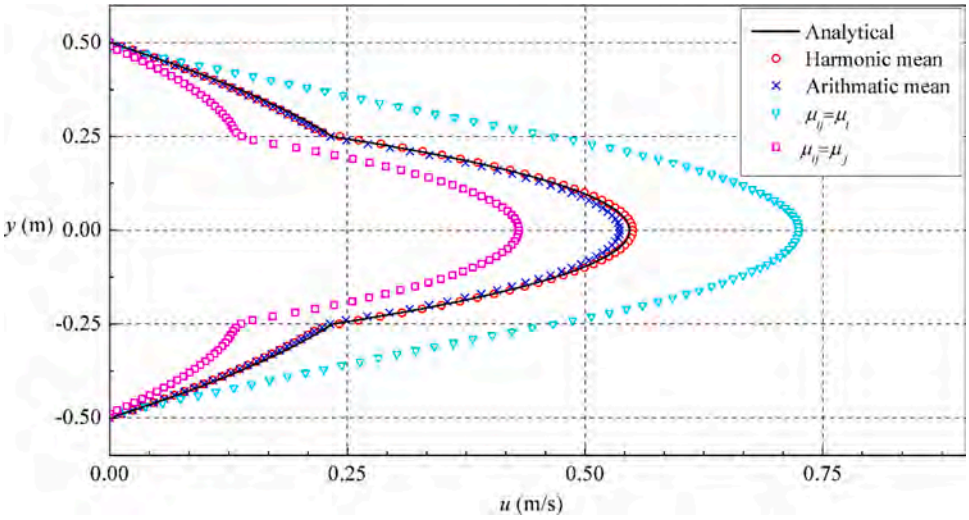

Fig. 3. Comparison of velocity profiles with different inter-particle viscosities for $M = 4$.

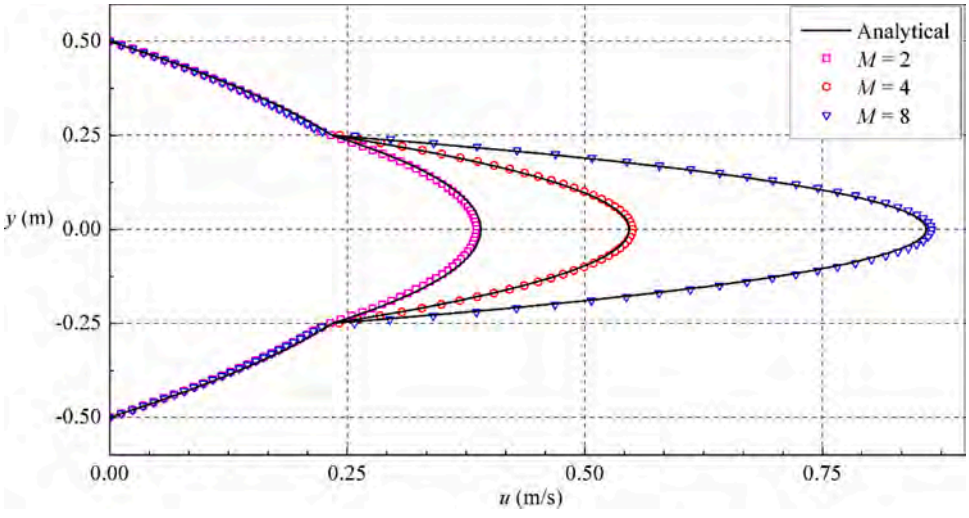

Fig. 4. Comparison of velocity profiles for $M = 2, 4, 8$, with the harmonic mean inter-particle viscosity.

method is mainly applied to single-phase simulation and suffers from unphysical pressure oscillations. If the multiphase method is directly developed on the basis of the original MPS method, the pressure oscillation would cause the inaccuracy of particle motion and unphysical penetration between different phases. Besides, the calculation efficiency of MPS method is relatively low due to the high computational cost on searching of neighbor particle and solving of PPE, which seems to be impossible to deal with the more complicated calculation process and

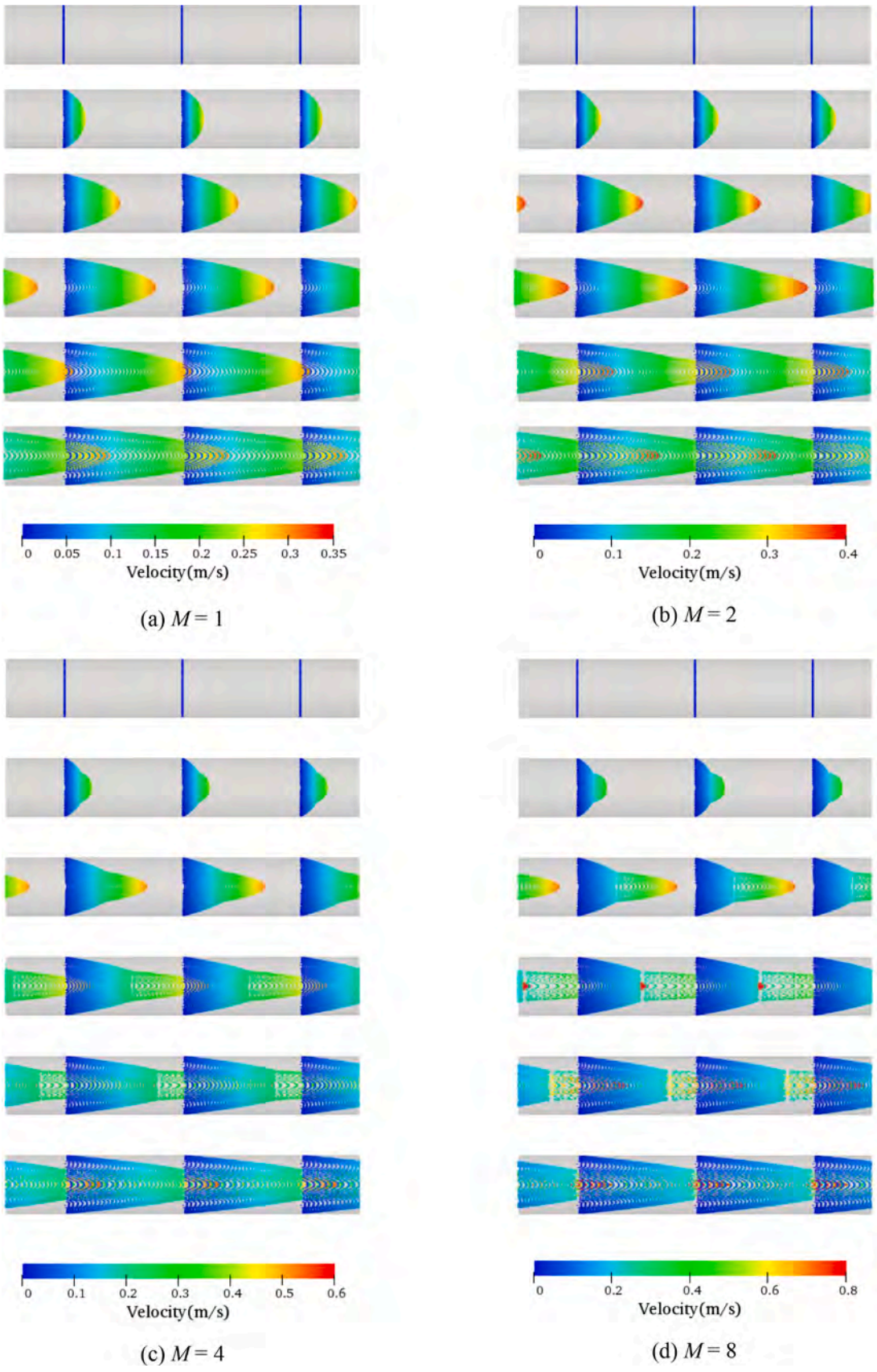

Fig. 5. MPS snapshots of multiphase Poiseuille flows with different viscosity ratios at $t = 0$ s, 2 s, 4 s, 6 s, 8 s, and 10 s, respectively.

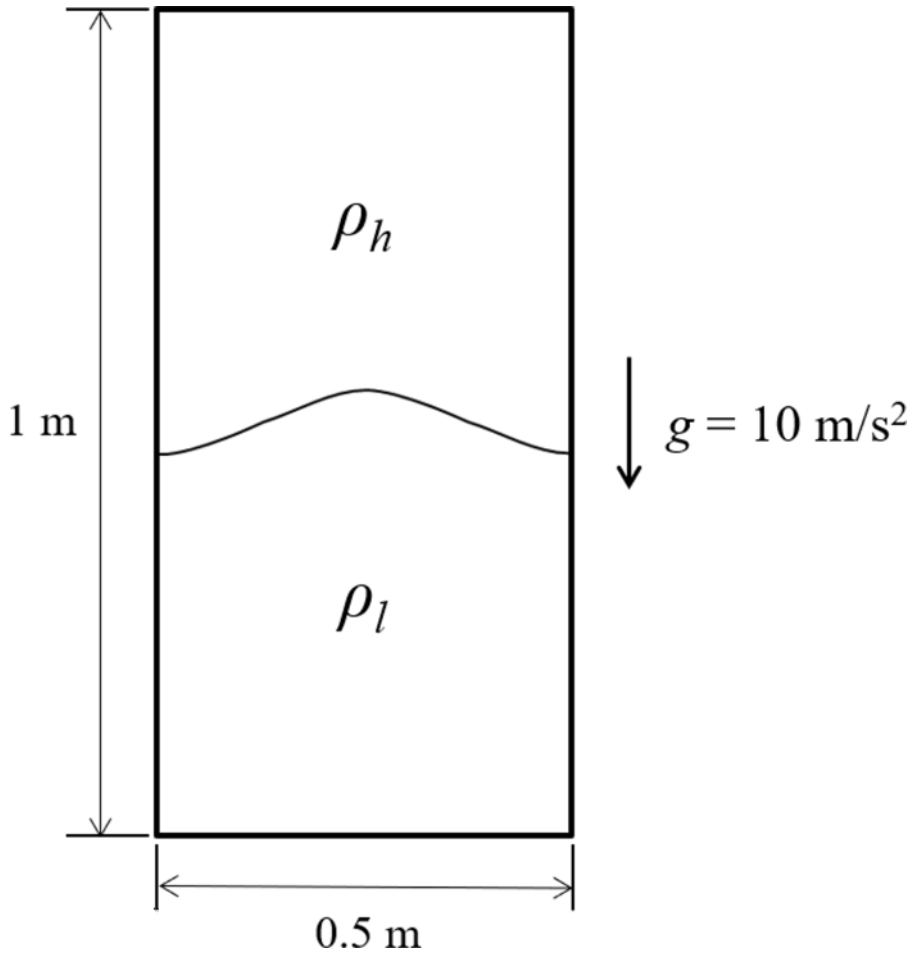

Fig. 6. Schematic diagram of 2-D Rayleigh-Taylor instability.

the sharp increase of particle number in the multiphase simulation. Therefore, most of the existing MPS studies simplified the fluid system to a single-phase model, in which the air region is assumed to be a vacuum and the effect of air phase is directly ignored. With this simplification, the single-phase MPS method becomes applicable for some interfacial flows, and in some cases, yields good agreement with the results of experiments. However, the accuracy of single-phase MPS simulations decreases with the increase of flow intensity. As can been observed in some experiments (Hu and Sueyoshi, 2010; Lobovský et al., 2014), a massive amount of air is trapped by backward plunging breaker in the violent dam-break flow and has significant influence on the shape of interface, which cannot be considered by using the single-phase MPS method. Moreover, the MPS method becomes completely unavailable for the multiphase problems with all fluids non-negligible, such as interface instability flow, bubbly flow, internal wave flow, etc.

In order to improve the accuracy and stability of MPS method, scholars have made a lot of optimizations on the numerical schemes of MPS in recent years (e.g., Khayyer and Gotoh, 2009a, 2010; Tanaka and Masunaga, 2010; Khayyer and Gotoh, 2011; Lee et al., 2011). Especially, an improved moving particle semi-implicit (IMPS, Zhang and Wan, 2017) has been proposed, which includes four improved schemes: first, kernel function without singularity (Zhang and Wan, 2012); second, momentum conservative gradient model (Tanaka and Masunaga, 2010); third, mixed source term for PPE (Tanaka and Masunaga, 2010); and fourth, highly precise free surface detection approach (Zhang and Wan, 2012). The comparison with the original MPS method (Zhang and Wan, 2017) shows that the pressure field simulated by IMPS method is smooth and stable, without unphysical pressure oscillation observed. Furthermore, the computational efficiency of IMPS method is also improved through the development and application of a series of acceleration techniques. In terms of software acceleration techniques, multi-resolution particle technique (Tang et al., 2016a) and overlapping particle technique (Tang et al., 2016b) are developed respectively, in which the local encryption is adopted instead of global encryption, reducing the total number of particles required to achieve the same accuracy. In terms of hardware acceleration techniques, GPU (Graphics Processing Unit) technique is employed (Chen and Wan, 2019a, 2019b), which is suitable for large-scale parallel computing due to the multi-core architecture of GPU device.

With the improvement of accuracy, stability and efficiency, the preconditions for extending the MPS method to multiphase flows are available. In recent years, some multiphase models have been gradually proposed and introduced into MPS. For example, Shakibaeinia and Jin (2012) introduced the density smoothing scheme into their WC-MPS method to solve the discontinuity of pressure on phase interface, with which the multiphase flows with low density ratios are simulated. Khayyer and Gotoh (2013) replaced the zero-order density smoothing scheme with a first-order density smoothing scheme, with which the sharpness of density variations across the interface is better maintained and the multiphase flows with high density ratios can be accurately simulated. Through the locally weighted average of interaction acceleration between particles, Duan et al. (2017) proposed a stable multiphase MPS method capable to fully guarantee the continuities of acceleration and velocity fields. Shimizu et al. (2018) developed an MPS-based particle method for multiphase flows characterized by high density ratios, by incorporating the concept of Space Potential Particles (SPP). To avoid the unphysical penetration in interfacial flows, the Optimized Particle Shifting (OPS) method developed by Khayyer et al.

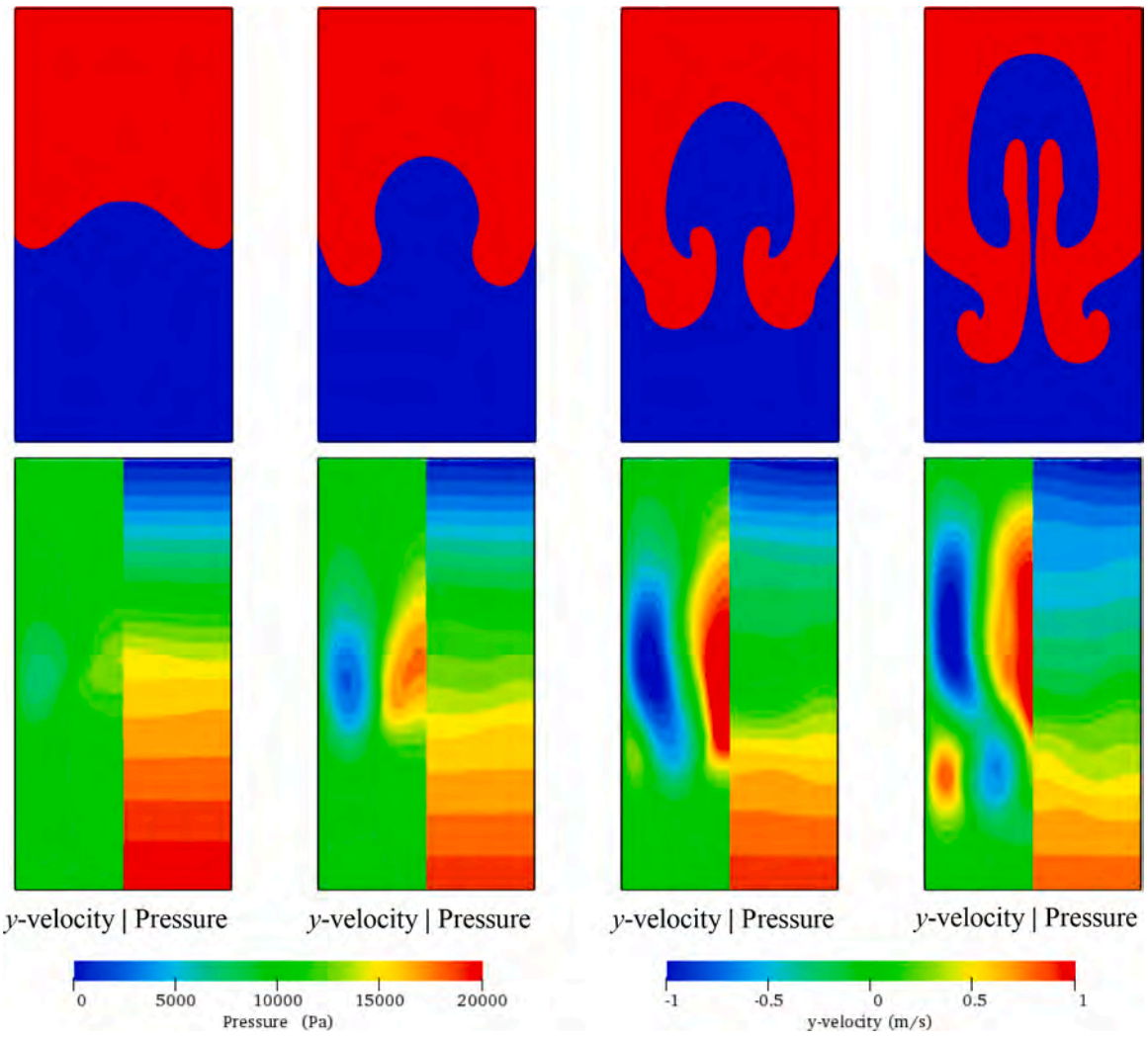

Fig. 7. Simulations results of Rayleigh-Taylor instability obtained by multiphase MPS method at $t(\lambda/g)^{-1/2} = 1.1$, 2.2, 3.3, and 4.4, from left to right.

(2017a) for free-surface flows is further extended to the multiphase flows to stabilize the interface (Khayyer et al., 2019). The surface tension models for MPS method are respectively proposed by Nomura et al. (2001) and Duan et al. (2015), which are crucially important for the interface capturing in the problems dominated by surface tension force.

In this paper, we aim to develop the IMPS method into a multiphase method, and to explore the advantages of MPS method in the simulation of interfacial flow. To achieve this goal, a series of widely validated multiphase models are introduced into IMPS method, such as the multi-density model, multi-viscosity model, continuous acceleration model, contoured continuum surface force (CCSF) model, etc., which would be presented in detail together with the basic concept of IMPS method in Section 2 and Section 3. Meanwhile, the GPU acceleration technique would be included in the developed multiphase MPS method to deal with the huge computational cost. Benefitting from the high stability and accuracy of IMPS method and the improvement by the multiphase models, the developed multiphase MPS method is successfully applied to a wide variety of 2-D/3-D interfacial flows in Section 4, including Rayleigh-Taylor instability, bubble rising, dam-break flow, and internal solitary waves. The simulation results are compared with other numerical and experimental results, through which the capacity of the present multiphase MPS method to capture complex interface is validated. The phenomenon of air entrapment induced by dam-break flow is also well reproduced and its influence on impact pressure is discussed in detail. Moreover, the energy conservation of the multiphase MPS method is further tested by the simulation of internal solitary waves with a long-distance propagation.

2. Improved MPS method

2.1. Governing equations

The governing equations of MPS method consist of equations for the conservation of mass and momentum (Koshizuka and Oka, 1996), with the following Lagrangian forms:

$$\frac{\mathrm{D}\rho}{\mathrm{Dt}} = -\rho(\nabla\cdot\mathrm{u}) \tag{1}$$

$$\rho\frac{\mathrm{Du}}{\mathrm{Dt}} = -\nabla\mathrm{P} + \mathrm{F}^{\mathrm{V}} + \mathrm{F}^{\mathrm{B}} + \mathrm{F}^{\mathrm{S}} \tag{2}$$

where ρ, u, and P represent the density, velocity, and pressure of the particles, respectively, and $\boldsymbol{F}^{V}$, $\boldsymbol{F}^{B}$, and $\boldsymbol{F}^{S}$ denote the viscous force, body force, and surface tension forces, respectively. Note that, the surface tension force $\boldsymbol{F}^{S}$ is usually ignored in the single-phase IMPS simulation.

2.2. Kernel function

There are various forms of interactions between neighboring particles in the MPS method, and the kernel function is used as a weight function to measure the strength of interactions. In the IMPS method,

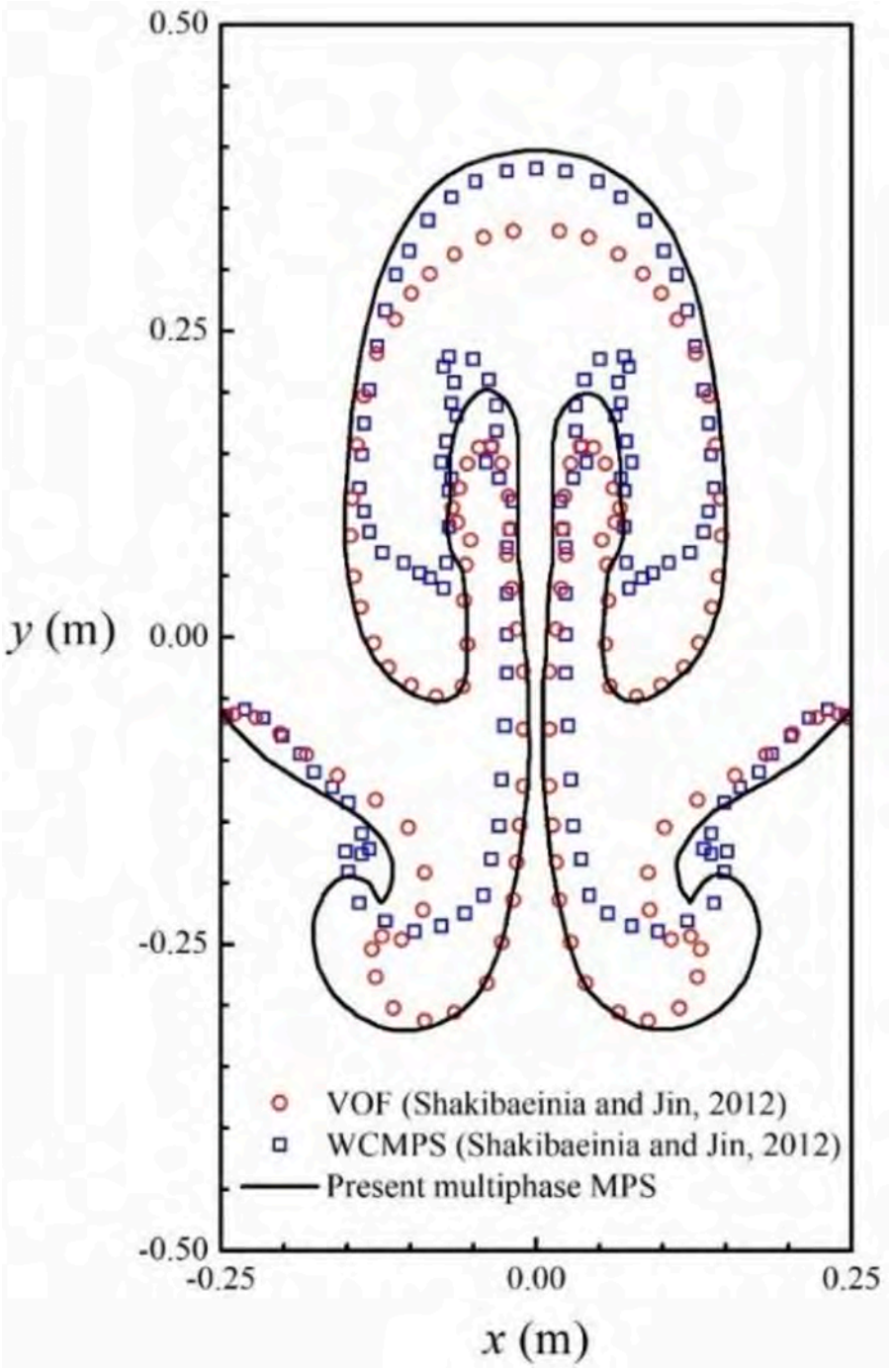

Fig. 8. Shape of phase interface in Rayleigh-Taylor instability captured by different methods at $t(\lambda/g)^{-1/2} = 4.4$.

the improved kernel function suggested by Zhang and Wan (2012) is used:

$$W\left(r_{ij}, r_e\right) = \begin{cases} \dfrac{r_e}{0.85r_{ij} + 0.15r_e} - 1 \ (0 \le r < r_e) \\ 0 \ (r_e \le r) \end{cases} \tag{3}$$

where r_{ij} and r_e represent the distance between particles and the largest radius of particle interaction, respectively. As the distance between particles decreases, the value of kernel function increases, resulting in the stronger particle interactions, and vice versa. When the particle distance is higher than a certain threshold, the kernel function becomes zero and the interaction disappears. The improved kernel function obtains a finite value when the distance becomes zero, thus the problem of singularity in the original kernel function (Koshizuka and Oka, 1996) can be avoided.

2.3. Particle interaction models

Models of particle interaction (Koshizuka and Oka, 1996) are used to discretize the differential operators in the governing equations, including the gradient model, divergence model, and Laplacian model, defined as:

$$< \nabla\phi >_i = \frac{D}{n^0} \sum_{j \neq i} \frac{\phi_j - \phi_i}{|r_j - r_i|^2} \left(r_j - r_i\right) \cdot W(r_{ij}, r_e) \tag{4}$$

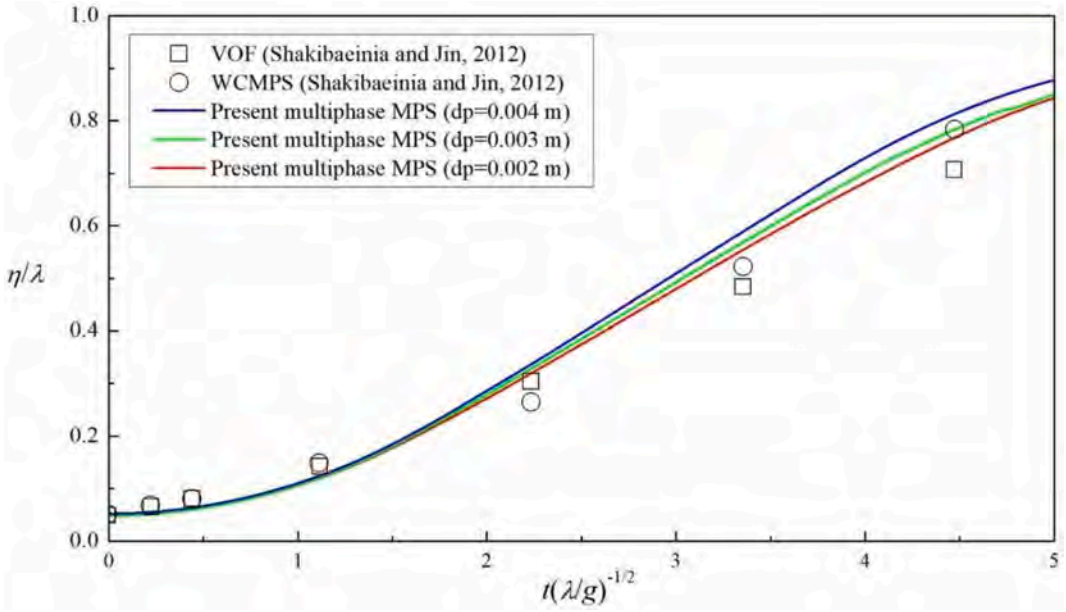

Fig. 9. Time evolution of maximum interfacial displacement in Rayleigh-Taylor instability.

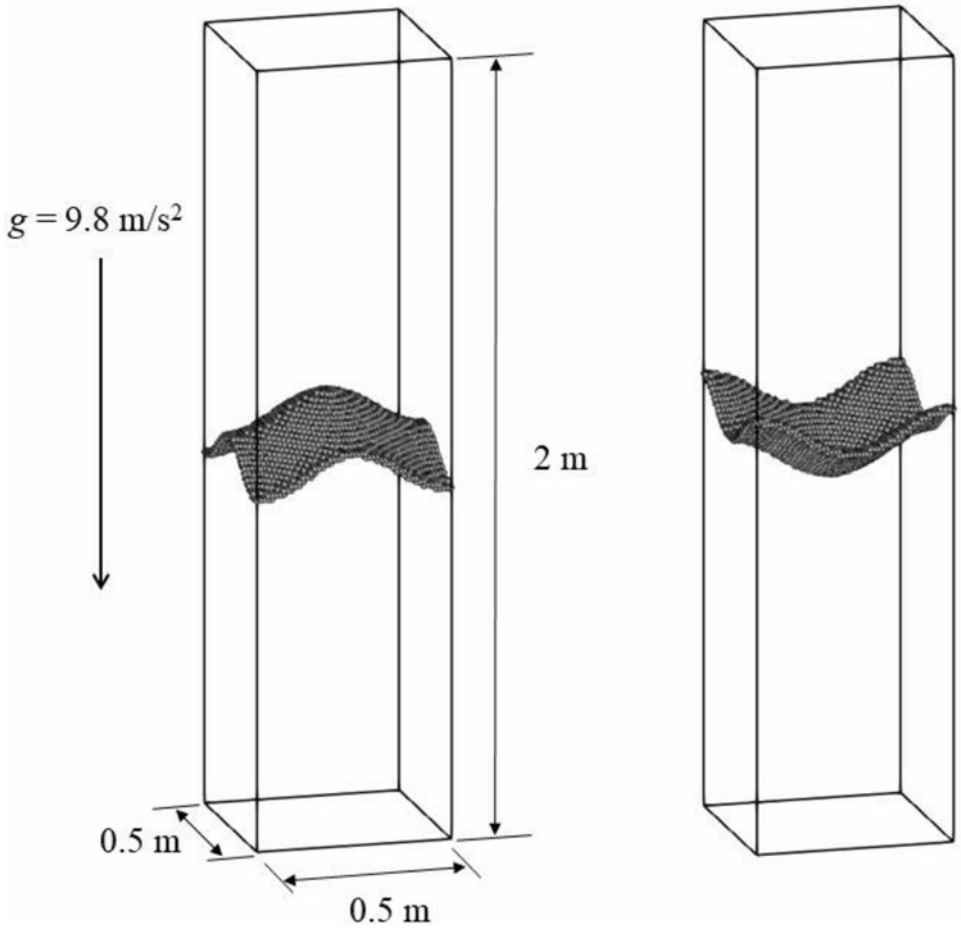

Fig. 10. Schematic diagram of 3-D Rayleigh-Taylor instability with different initial disturbances.

$$< \nabla\Phi >_i = \frac{D}{n^0}\sum_{j\neq i}\frac{(\Phi_j - \Phi_i)}{|r_j - r_i|^2}(r_j - r_i)\cdot W(r_{ij}, r_e)\Bigg) \quad (5)$$

$$< \nabla^2\phi >_i = \frac{2D}{n^0\lambda}\sum_{j\neq i}(\phi_j - \phi_i)\cdot W(r_{ij}, r_e) \quad (6)$$

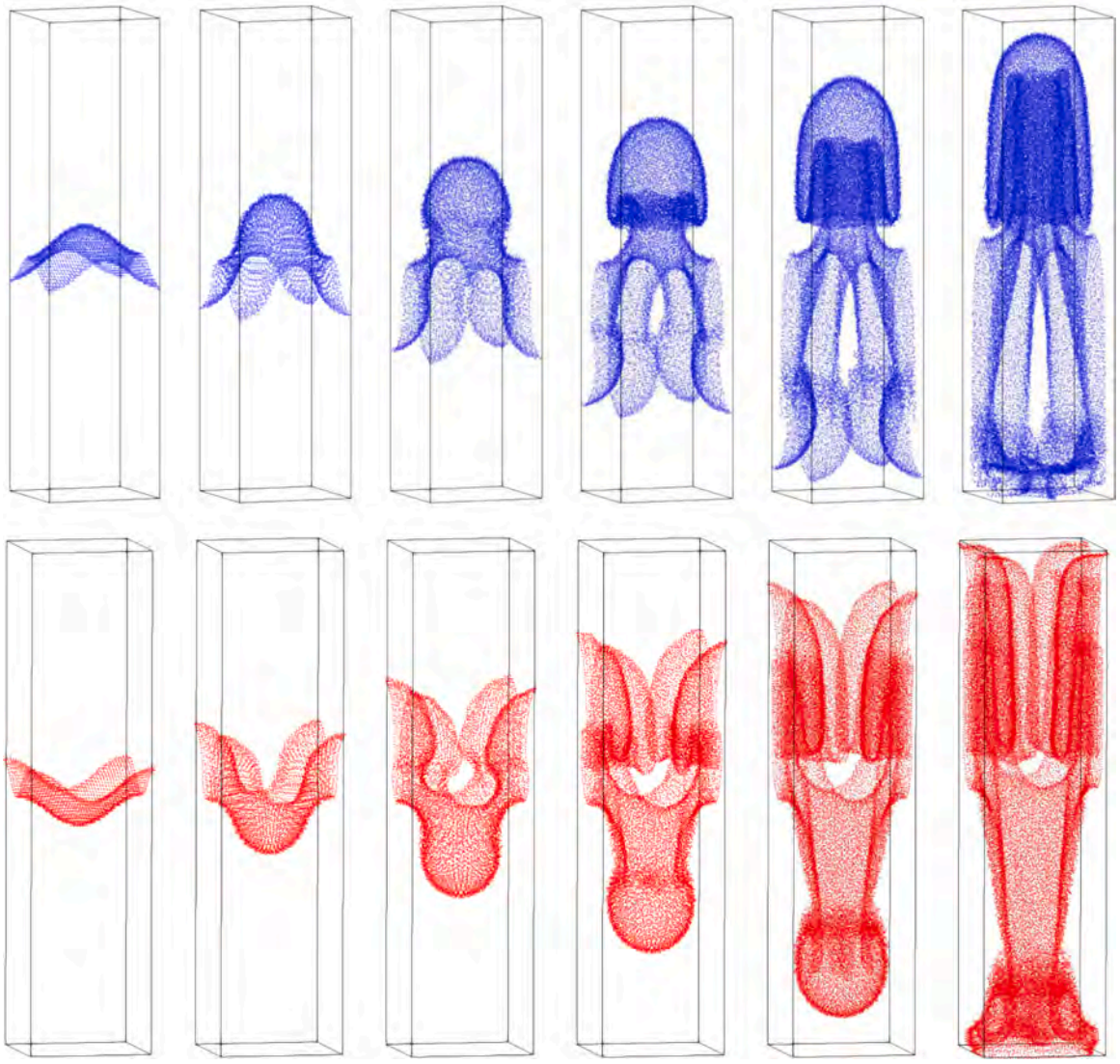

Fig. 11. Evolutions of phase interface in 3-D Rayleigh-Taylor instability with the convex (top) or concave (bottom) initial disturbance at $t = 0$ s, 0.3 s, 0.5 s, 0.7 s, 0.9 s, 1.1 s.

where ϕ is an arbitrary scalar function, $\boldsymbol{\Phi}$ is an arbitrary vector, D is the number of spatial dimensions, n^0 is the particle number density with the initial arrangement, calculated as:

$$< n >_i = \sum_{j \neq i} W(r_{ij}, r_e) \tag{7}$$

and λ is a parameter to keep the increase in variance equal to that in the analytical solution. It is calculated as:

$$\lambda = \frac{\sum_{j \neq i} W(r_{ij}, r_e) \cdot |r_j - r_i|^2}{\sum_{j \neq i} W(r_{ij}, r_e)} \tag{8}$$

2.4. Pressure gradient model

When the gradient model given in Eq. (4) is applied to calculate the pressure gradient force, the conservation of linear and angular momenta cannot be fully satisfied, and the significant tensile instability (Koshizuka et al., 1998) may be caused. To overcome this, modifications and corrections are made by Khayyer and Gotoh (2008), and the first momentum conservative gradient model for MPS is proposed. In the IMPS method, the following conservative form proposed by Tanaka and Masunaga (2010) is used:

$$< \nabla P >_i = \frac{D}{n^0} \sum_{j \neq i} (P_j + P_i) \frac{(r_j - r_i)}{|r_j - r_i|^2} \cdot W(r_{ij}, r_e) \tag{9}$$

With the above model, the pure repulsive force between particles can be guaranteed, thus the problem of tensile instability is solved.

2.5. Semi-implicit algorithm

To maintain the incompressibility of fluid, a semi-implicit algorithm is used in the MPS method, in which each time step is divided into the first prediction step and the second correction step. As mentioned above, this is also the main difference between MPS and SPH for a long time. In the prediction step, the temporal velocity field is explicitly updated according to the viscous force, gravitational force, and possible surface tension force. In the correction step, the PPE is solved to obtain the pressure field, through which the velocities and locations of particles are finally updated to the next time step. In the IMPS method, the PPE with a mixed source term is used, which is proposed by Tanaka and Masunaga (2010) and rewritten by Lee et al. (2011):

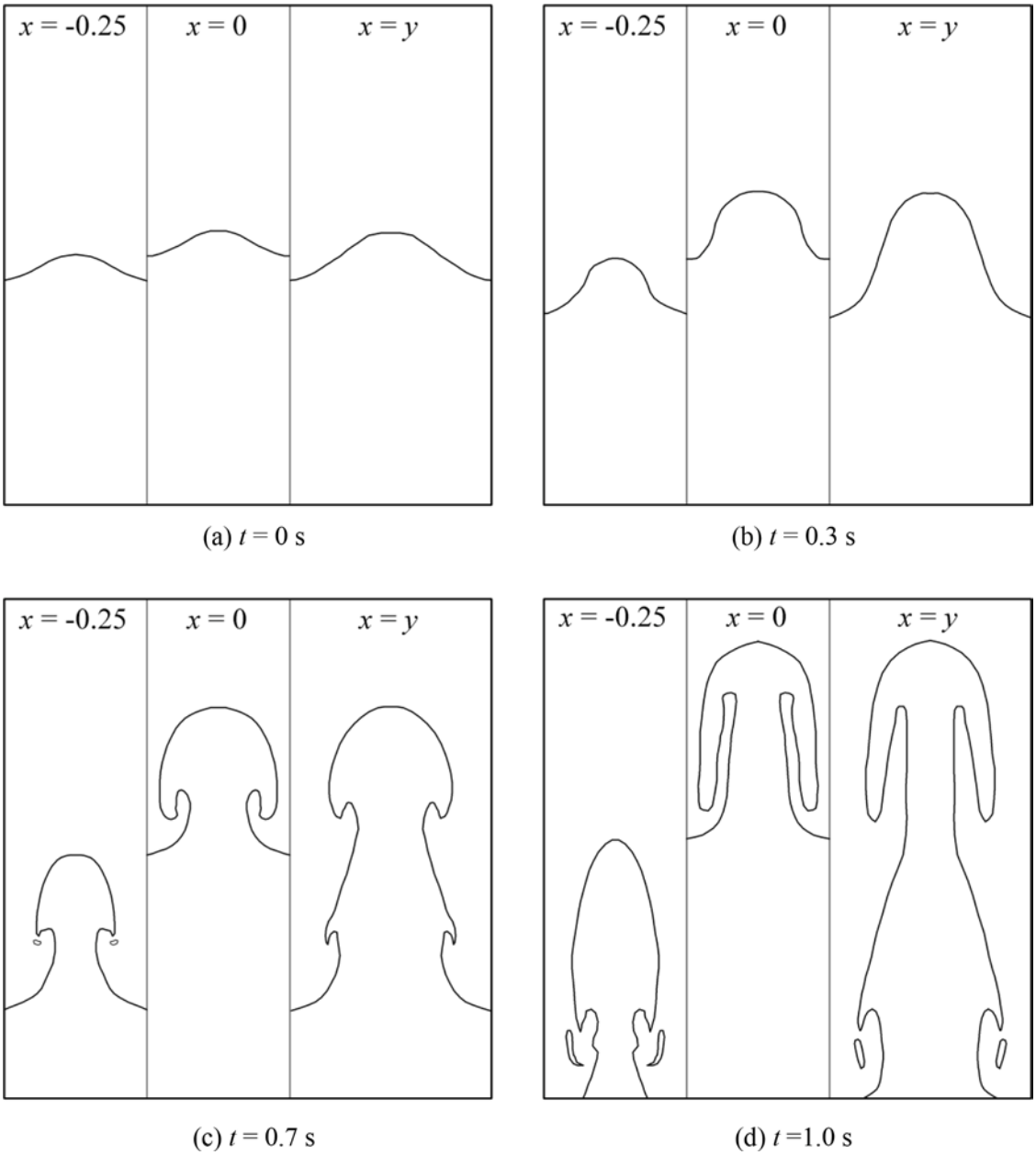

Fig. 12. Cross-sectional views of phase interface in 3-D Rayleigh-Taylor instability with the convex initial disturbance at three vertical planes, $x = -0.25$, $x = 0$, and $x = y$.

$$< \nabla^2 P^{k+1} >_i = (1 - \gamma)\frac{\rho}{\Delta t}\nabla \cdot u_i^* - \gamma\frac{\rho}{\Delta t^2}\frac{< n^k >_i - n^0}{n^0} \tag{10}$$

where γ is a blending parameter less than 1, $\boldsymbol{u}_i^*$ is the temporal velocity, and $<n^k>_i$ is the particle number density at the k^{th} time step. As Tanaka and Masunaga (2010) indicated, the mixed source term is in fact a combination of the divergence-free incompressible condition and the incompressible condition for particle number density, which is favorable for the suppression of pressure oscillations. According to the numerical tests about the value of γ by Lee et al. (2011), error of the numerical pressure can be reduced while $\gamma = 0.01$ which is also used in present paper. In fact, there are already some algorithms that can avoid tuning parameter, such as the ECS scheme of Khayyer and Gotoh (2011) with dynamic coefficients as functions of instantaneous flow field, which are hopefully applied in our future work.

2.6. Boundary conditions

With regard to the free surface, a Dirichlet boundary condition of zero pressure is imposed to the free surface particles. To accurately identify all free surface particles, the IMPS method employs s a highly precise approach (Zhang and Wan, 2012), in which a vector is defined to quantitatively assess the asymmetry of particle distribution:

$$F_i = \frac{D}{n^0}\sum_{j \neq i}\frac{(r_i - r_j)}{|r_i - r_j|} \cdot W(r_{ij}, r_e)\Bigg) \tag{11}$$

For free surface particles, all neighboring particles are located on the liquid side. Therefore, the high asymmetry and low particle number density are considered as the main two criteria in this approach, and particles satisfying the following conditions are judged to be free surface particles:

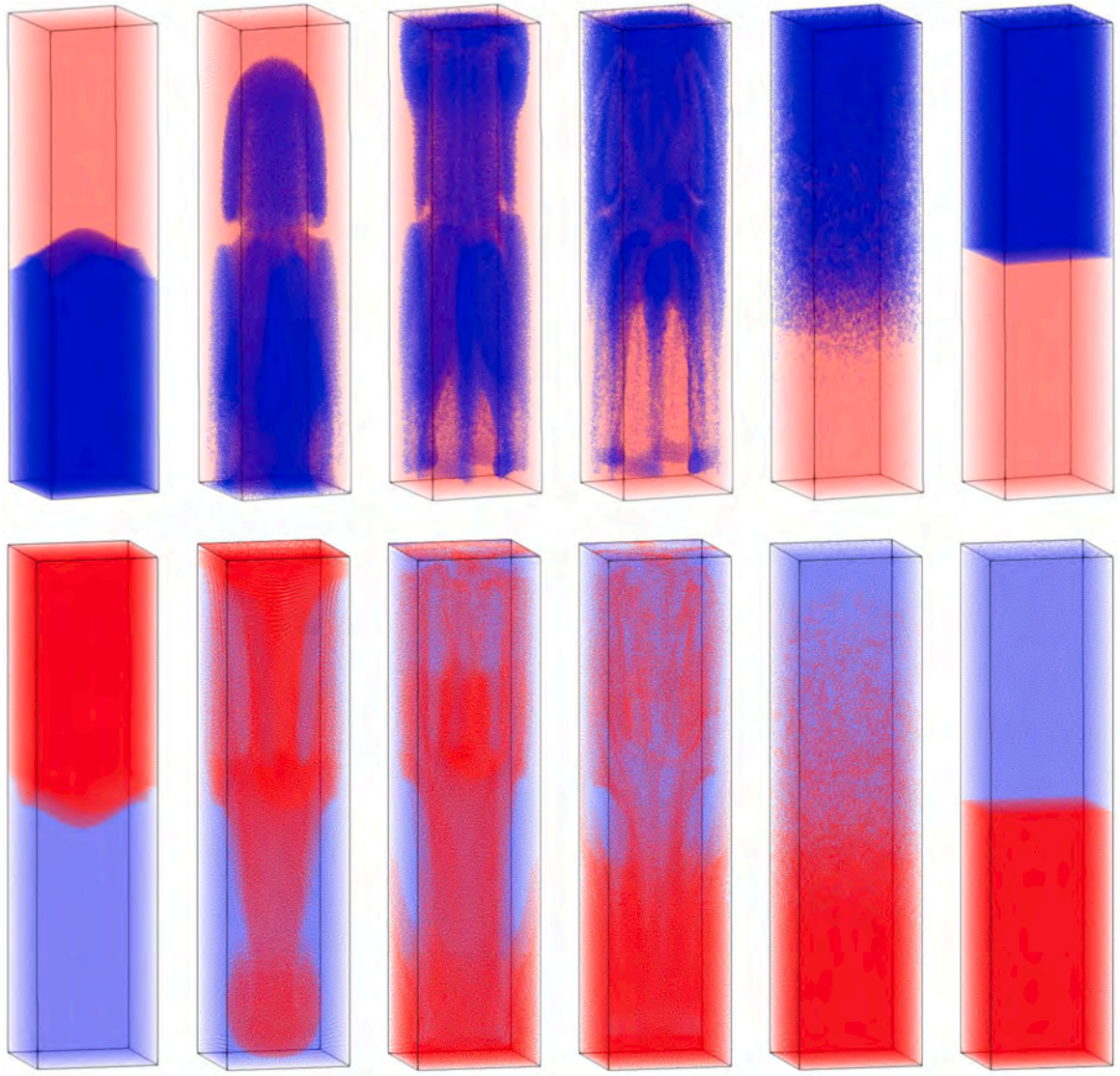

Fig. 13. Phase fields in 3-D Rayleigh-Taylor instability with the convex (top) or concave (bottom) initial disturbance at $t = 0$ s, 0.5 s, 1 s, 1.5 s, 5 s, 30 s.

$$< n >_i \; < \beta_1 n^0 \text{ or } \left(< n >_i \; > \; \beta_1 n^0 \text{ and } < n >_i \; < \; \beta_2 n^0 \text{ and } |F|_i \; > \alpha |F^0|\right) \tag{12}$$

where $\alpha = 0.9$, $\beta_1 = 0.8$, and $\beta_2 = 0.97$. The above detection approach follows the basic principle of the so-called ASA (Assessment of free-surface on the basis of nearly Symmetric Arrangement of non-free-surface particles) scheme, which was initially developed and applied to SPH method (Khayyer and Gotoh, 2009b; Khayyer et al., 2009).

3. Multiphase MPS method

3.1. Improved density smoothing scheme

For interfacial flows, the density field is mathematically discontinuous at the phase interface. To overcome the numerical instability induced by this discontinuity, an improved density smoothing scheme is employed by our multiphase MPS method. Firstly, a transition region is defined in the vicinity of the phase interface. Then, the spatially weighted average density of particles inside the transition region is calculated using the following formula:

$$< \rho >_i \; = \; \frac{\rho_i W_{self} + \sum_{j \in I} \rho_j W(r_{ij}, r_e)}{W_{self} + \sum_{j \in I} W(r_{ij}, r_e)} \tag{13}$$

where I includes the target particle i and all its neighboring particles, and W_{self} is a weight function used to magnify the influence of the target particle itself so that the smoothed density field is closer to the real density field. The principle of this improvement is similar with the first-order smoothing scheme proposed by Khayyer and Gotoh (2013). Compared with the original scheme (Shakibaeinia and Jin, 2012) proposed for problems with low density ratios, the improved scheme can better maintain the sharpness of the variation in density, thus some flow characteristics associated with the high density ratios can be captured more accurately.

3.2. Inter-particle viscosity model

There exists also a discontinuity of viscosity field at the phase interface, which would significantly affect the calculation accuracy of viscous force between particles inside the transition region. To deal with this, the inter-particle viscosity model (Shakibaeinia and Jin, 2012) is employed in the present multiphase MPS method. Specially, when

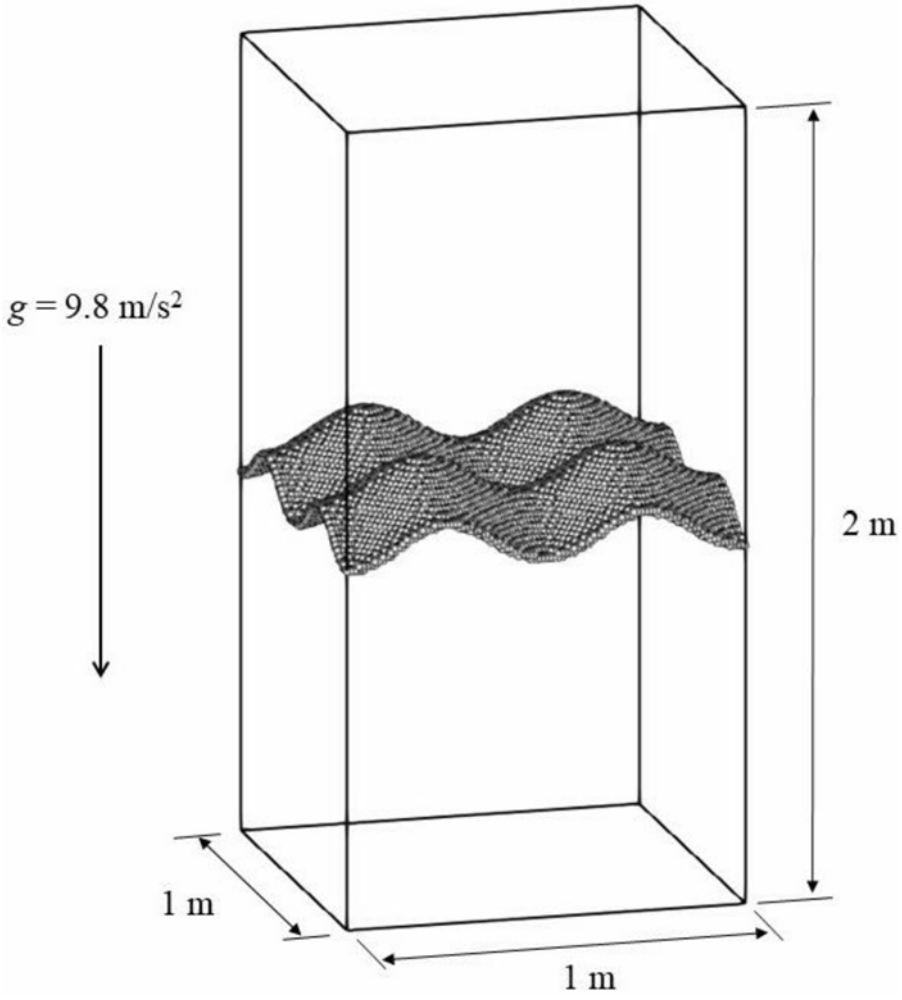

Fig. 14. Schematic diagram of 3-D multi-mode Rayleigh-Taylor instability.

particles belonging to different phases interact with each other, the inter-particle viscosity would be applied to substitute the viscosity of real particles during the calculation of viscous forces. The value of inter-particle viscosity is obtained by averaging the viscosities of a pair of interacting particles:

$$\mu_{ij} = \left[(\mu_i^{\theta} + \mu_j^{\theta})/2 \right]^{1/\theta} \tag{14}$$

where μ_{ij} represents the inter-particle viscosity, μ_i and μ_j represent the dynamic viscosities of particles i and j, respectively, and θ is a parameter determining the averaging method. For $\theta = 1$, the arithmetic mean is used. For $\theta = -1$, the harmonic mean is used. Recommended by Shakibaeinia and Jin (2012), the harmonic mean of the inter-particle viscosity is used in the present multiphase MPS method, with which the viscosity term in the dovering equations turns into the following form:

$$F^V = \mu\nabla^2 u = \frac{2D}{n^0\lambda}\sum_{j\neq i}\frac{2\mu_i\mu_j}{\mu_i + \mu_j}\left(u_j - u_i\right)\cdot W(r_{ij}, r_e) \tag{15}$$

3.3. PPE with inter-particle density

In the transition region, the pressure field is likely to suffer from an enormous change owing to the rapid variation of density field. Therefore, an unphysically large pressure gradient may be generated and causes the interface particles to move violently, especially for lighter particles, which reduces the numerical stability finally. To maintain the smoothness of pressure field, the PPE with inter-particle density (Duan et al., 2017) is used in the present multiphase MPS method. Using it, the left-hand side of the PPE is discretized as:

$$< \frac{1}{\rho_{ij}}\nabla^2 P^{k+1} >_i = \frac{2D}{n^0\lambda}\sum_{j\neq i}\frac{1}{\rho_{ij}}\left(P_j^{k+1} - P_i^{k+1}\right)\cdot W(r_{ij}, r_e) \tag{16}$$

where ρ_{ij} is the inter-particle density with a definition similar to μ_{ij} in Eq. (14), but the arithmetic mean is used here according to numerical tests by Duan et al. (2017), written as:

$$\rho_{ij} = \frac{\rho_i + \rho_j}{2} \tag{17}$$

3.4. Modified pressure gradient model for high density ratios

When calculated according to the gradient model of single-phase MPS method, such as Eq. (4) or Eq. (9), the pressure gradient forces between a pair of interacting particles possess the same value. However, the consistency of forces would cause a significant discrepancy for the accelerations of particles with different densities. Specially, owing to the high density ratio, the acceleration of the lighter particles may be greatly

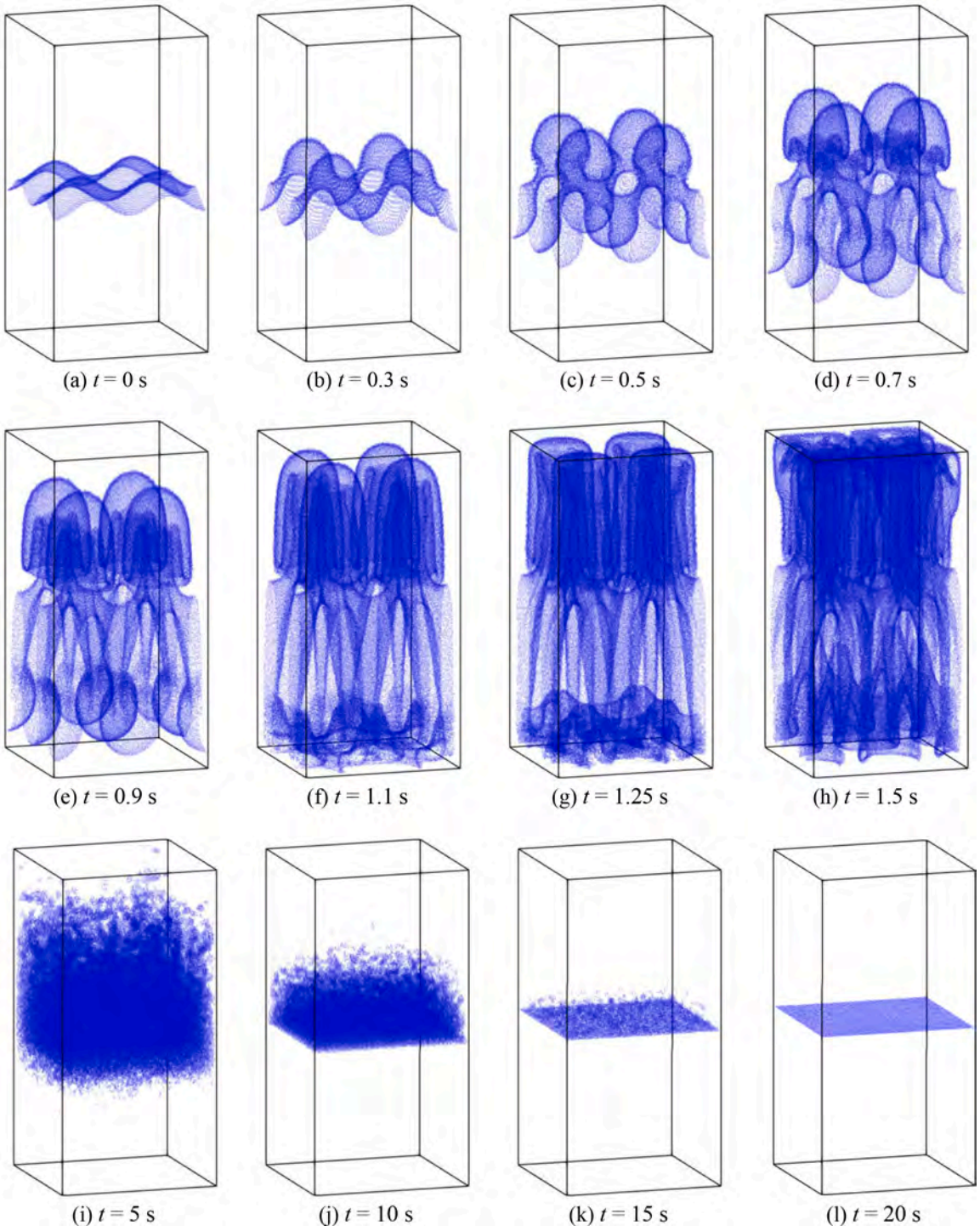

Fig. 15. Evolution of phase interface in 3-D multi-mode Rayleigh-Taylor instability.

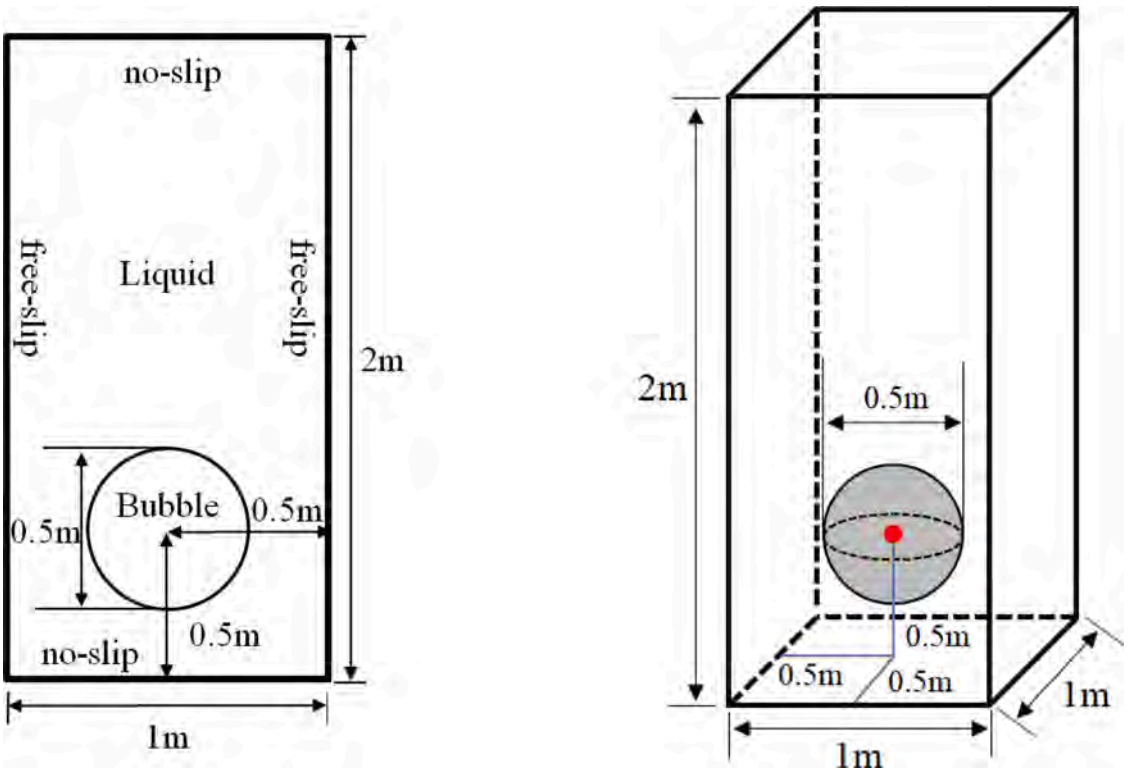

Fig. 16. Schematic diagram of 2-D/3-D bubble rising.

overestimated compared with that of the heavier particles, resulting in the discontinuity of acceleration field and numerical instability. In the present multiphase MPS method, the modified pressure gradient model (Duan et al., 2017) for high density ratios is introduced to obtain a continue and stable acceleration field:

$$<\frac{1}{\rho_{ij}}\nabla P>_i = \frac{D}{n^0}\sum_{j\neq i}\frac{2(P_j - P_i)}{\rho_i + \rho_j}\frac{(r_j - r_i)}{|r_j - r_i|^2}\cdot W(r_{ij}, r_e) + \frac{D}{n^0}\sum_{j\neq i}\frac{\left(P_i - P'_{i,min}\right)}{\rho_i}\frac{(r_j - r_i)}{|r_j - r_i|^2}\cdot W(r_{ij}, r_e)\Bigg) \quad (18)$$

where $P'_{i,min}$ represents the minimal pressure among the same-phase neighboring particles of particles *i*. The first term on the right-hand side of Eq. (18) is a modified form of the original pressure gradient model, in which the inter-particle density is introduced to maintain the consistency of particle accelerations. The second term is actually a vector with the same direction as the vector defined in Eq. (11), pointing from the denser particle region to the relatively dilute particles region. Therefore, it can be regarded as a particle-stabilizing term (PST), which is favorable for the uniform distribution of particles through the exertion of an artificial force.

3.5. Surface tension model

The surface tension effects are helpful to keep the phase interface clear by preventing nonphysical penetrations between phases. In the present multiphase MPS method, the continuum surface force (CSF) model proposed by Brackbill et al. (1992) is followed, in which the surface tension force is converted into a body force, calculated as:

$$F^S = -\sigma\kappa\nabla C \quad (19)$$

where σ is the coefficient of surface tension, κ is the curvature of the interface, and ∇C is the gradient of the artificially defined color function. To maintain the continuity of accelerations, the density-weighted color function (Zhang et al., 2015) is employed:

$$C_{ij} = \begin{cases} 0 \text{ if particles i and j belong to the same phase} \\ \frac{2\rho_i}{\rho_i + \rho_j} \text{ if particles i and j belong to different phases} \end{cases} \quad (20)$$

To gain the interface curvature κ, an analytical method proposed in the contoured continuum surface force (CCSF) model (Duan et al., 2015) is adopted here. The main idea is to approximate the phase interface by the contours of the smoothed color function. In the first step, the smoothed color function *f* at an arbitrary location (*x, y*) is obtain by the spatially weighted averaging of the original color function:

$$f(x, y) = \frac{\sum_{j\neq i} C_j G(r_{ij}, r_s)}{\sum_{j\neq i} G(r_{ij}, r_s)}, \quad G(r_{ij}, r_s) = \frac{9}{\pi r_s^2}\exp\left(-\frac{9 r_{ij}^2}{r_s^2}\right) \quad (21)$$

Then, the local contour passing through particle *i* is obtained by a Taylor series expansion:

$$f_{x,i}(x - x_i) + f_{y,i}(y - y_i) + \frac{1}{2}f_{xx,i}(x - x_i)^2 + f_{xy,i}(x - x_i)(y - y_i) + \frac{1}{2}f_{yy,i}(y - y_i)^2 = 0 \quad (22)$$

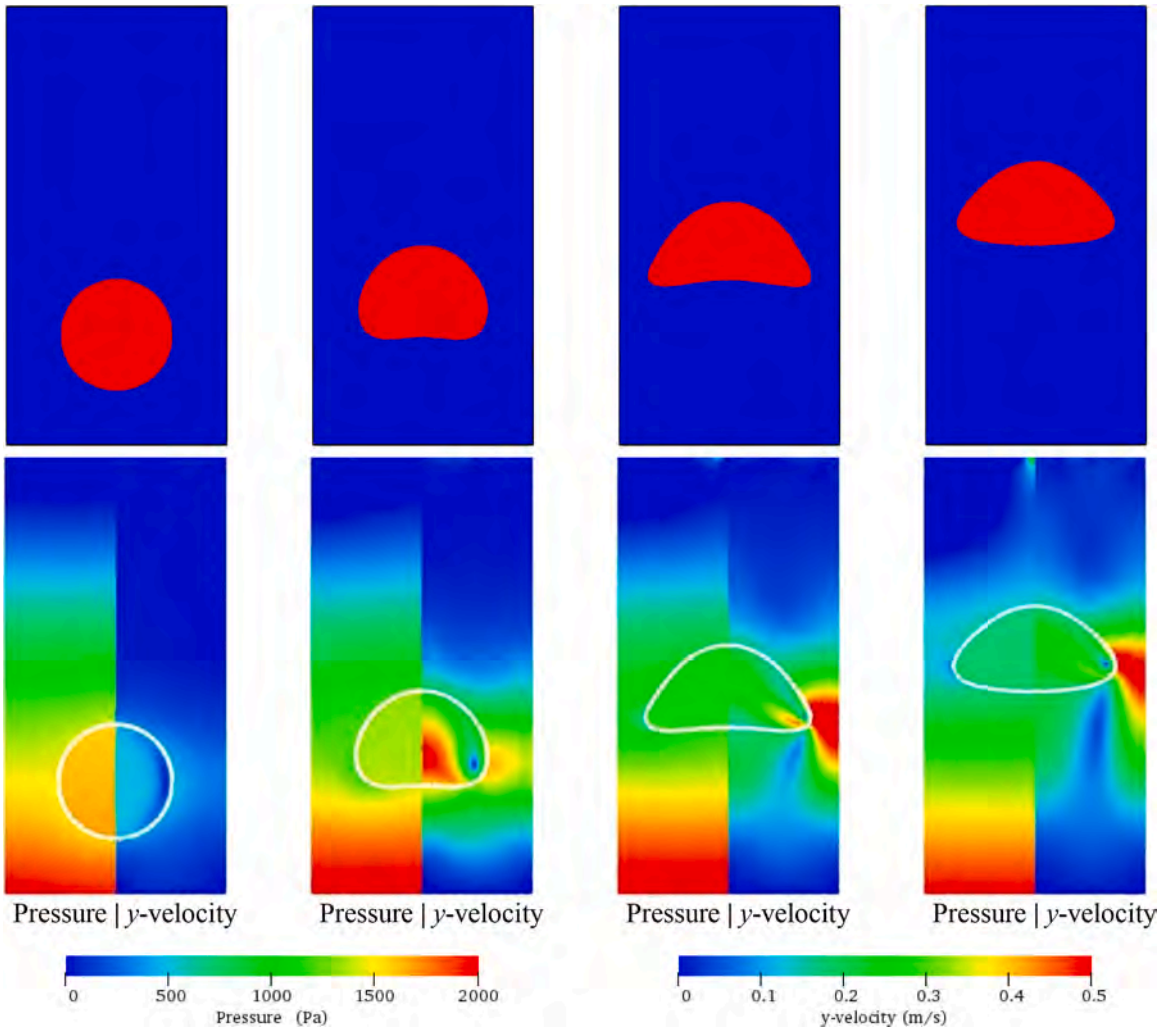

Fig. 17. Simulation results of bubble rising obtained by multiphase MPS method at $t = 0$ s, 1 s, 2 s, 3 s, from left to right.

where the subscripts x and y represent partial derivatives with respect to x and y, respectively.

Finally, the curvature of the interface at particle i can be analytically calculated as:

$$\kappa_i = \frac{y''}{\left(1+y_i'\right)^{3/2}} = \frac{2f_{x,i}\, f_{y,i}\, f_{xy,i} - f_{x,i}^2\, f_{yy,i} - f_{y,i}^2\, f_{xx,i}}{\left(f_{x,i}^2 + f_{y,i}^2\right)^{3/2}} \tag{23}$$

3.6. Multiphase particle collision model

The uniform distribution of particles is very important for the stability of MPS simulations. However, due to the randomness of particles motion, the particle distribution is difficult to maintain an ideal state throughout the numerical simulation and nonphysical penetrations may occur when too small particle spacing appears. In order to correct the particle distance, the multiphase collision model (Shakibaeinia and Jin, 2012) is introduced into the present multiphase MPS method, which assumes the occurrence of particle collisions once the particle distance is lower than a certain threshold. Based on the collision theory of two spheres with different masses, the velocities of particles after collision are updated as:

$$u_i' = u_i - \frac{1}{\rho_i}(1+\varepsilon)\frac{\rho_i\rho_j}{\rho_i+\rho_j}u_{ij}^n \tag{24}$$

$$u_j' = u_j + \frac{1}{\rho_j}(1+\varepsilon)\frac{\rho_i\rho_j}{\rho_i+\rho_j}u_{ij}^n \tag{25}$$

where u_{ij}^n is the normal relative velocity of particles i and j, u_i' and u_j' are the velocity vectors after collision, respectively, and ε represents the collision ratio which is equal to 0.5, as suggested by Shakibaeinia and Jin (2012).

3.7. Compressible-incompressible model

In some violent flows, the compression of air phase is likely to be induced by the strong impact of waves on walls of the tank. To reproduce this process, the compressible-incompressible model is applied in the present multiphase MPS method, which consider the water and air phases to be incompressible and compressible, respectively. Similar with the treatments of Khayyer and Gotoh (2016) and Duan et al. (2017), a compressibility term derived from the equation of state (EoS) is included into the PPE source term of the air particles:

$$<\nabla^2 P^{k+1}>_i = (1-\gamma)\frac{\rho}{\Delta t}\nabla\cdot u_i^* - \gamma\frac{\rho}{\Delta t^2}\frac{<n^k>_i - n^0}{n^0} + \frac{1}{\Delta t^2 C_s^2}P_i^{k+1} \tag{26}$$

where C_s is the physical speed of sound, same as that in Khayyer and Gotoh (2016). An extra benefit of the above scheme is that the compressibility term would be moved to the left-hand side of Eq. (26)

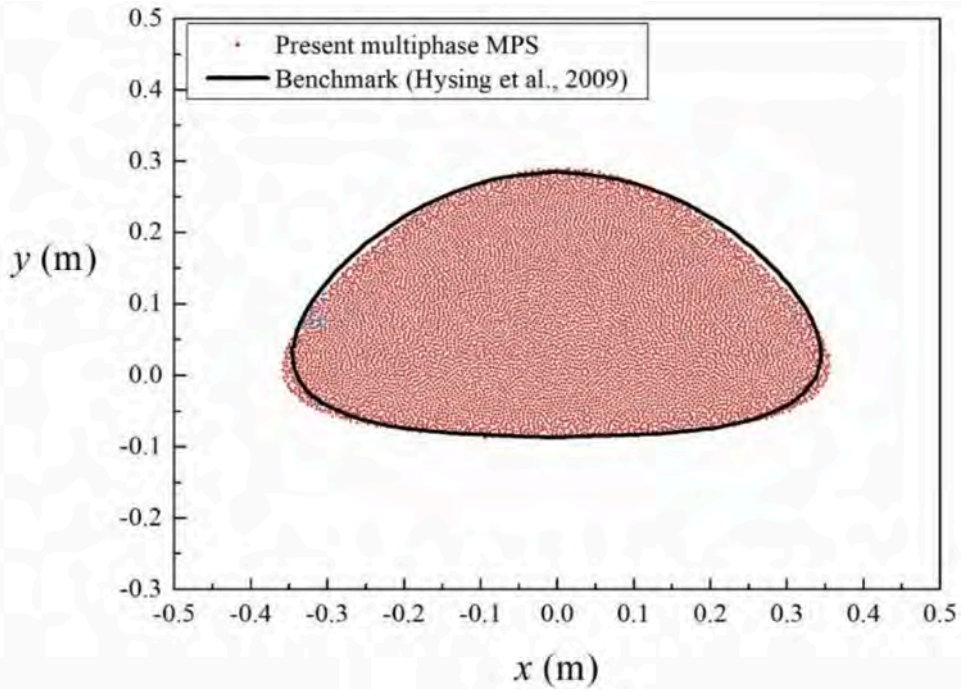

Fig. 18. Comparison of 2-D bubble shapes obtained by different methods, $t = 3$ s.

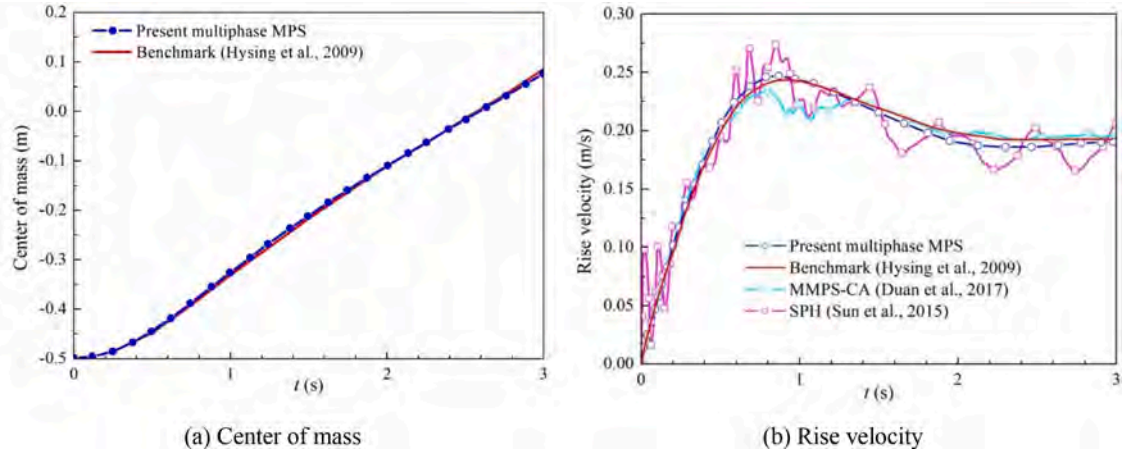

Fig. 19. Quantitative results obtained by multiphase MPS method in 2-D bubble rising and comparison with benchmark results and other numerical results.

while solving the PPE, which increases the values of diagonal elements of the coefficient matrix and improves the stability of the calculated pressure field (Tanaka and Masunaga, 2010). Note that, the compressible-incompressible model is activated only when the air phase becomes necessary to be considered, corresponding to the dam-break flow simulation in the subsequent application research.

3.8. GPU acceleration technique

Due to its multi-core architecture, GPU (Graphics Processing Unit) is quite suitable for high-performance parallel computing, and has been widely applied in large-scale simulations (Crespo et al., 2011; Zhao et al., 2017; Chow et al., 2018). As to MPS method, the GPU acceleration technique has been applied in the single-phase flows (Hori et al., 2011; Zhu et al., 2011; Xie et al., 2020), but there have been few studies on GPU applications in the multiphase MPS simulation.

In this paper, the GPU acceleration technique developed in IMPS method (Chen and Wan, 2019a and 2019b) is further extended and introduced into the present multiphase MPS method. Fig. 1 shows the flowchart of multiphase MPS method with GPU acceleration technique. As can be seen, both CPU and GPU are utilized but with different tasks. The CPU works as a host part to deal with logical works, environment configuration, instructions for setting parallelism and communicating data between CPU and GPU, while The GPU works as a device part responsible for all the parallel computing. Due to the simultaneous solution of different phase, the calculation process of multiphase MPS keep consistent with that of IMPS method, except for the addition of multi-phase models. Thus, the speedup of GPU for multiphase simulation can be considered as the same as that in single-phase simulation.

4. Numerical simulations

4.1. 3-D multiphase poiseuille flow

In the present multiphase MPS method, the inter-particle viscosity model is used to calculate the viscous force between particles of different

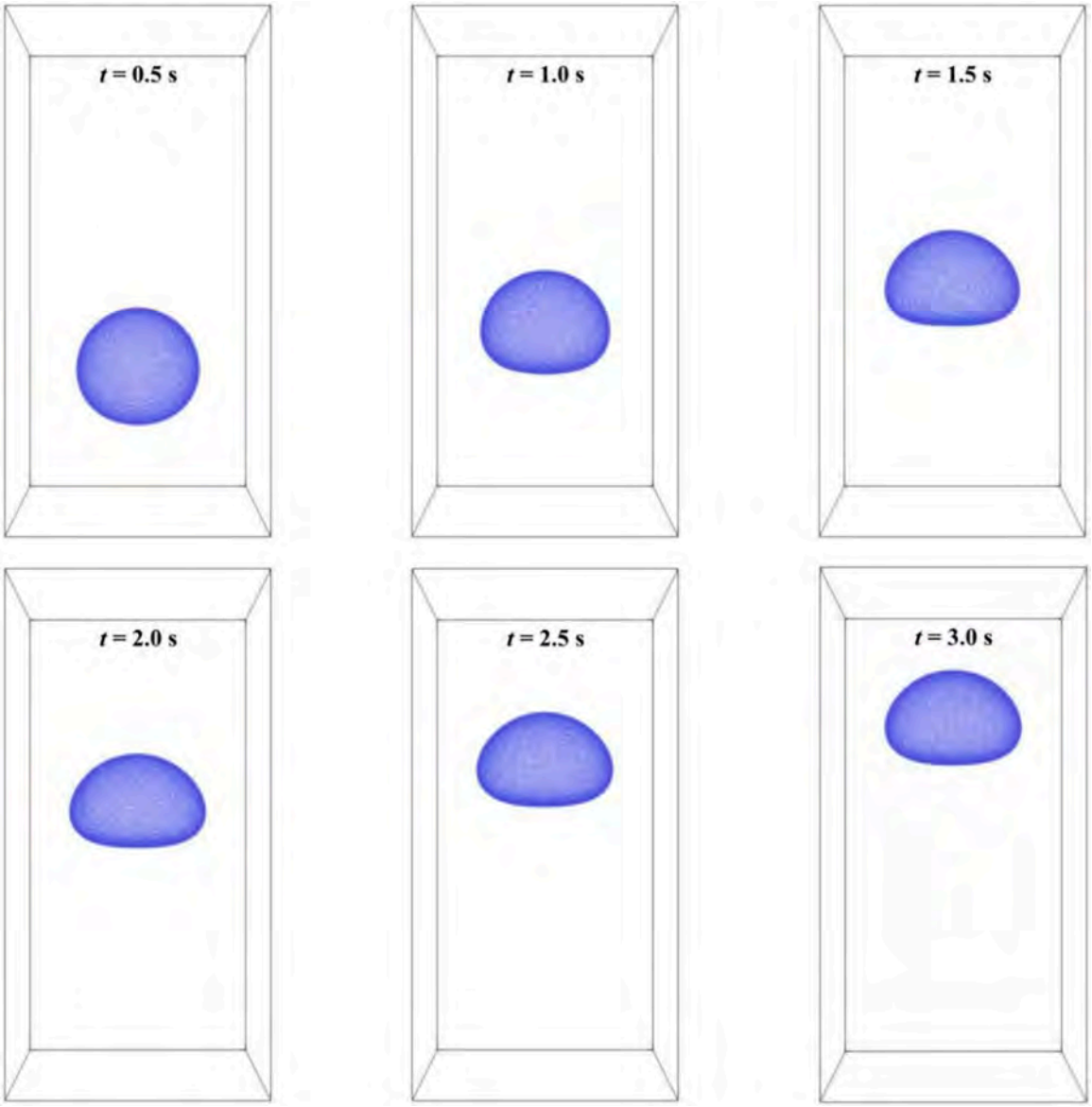

Fig. 20. Time evolution of the 3-D bubble shape simulated by multiphase MPS method.

phases. For the purpose of verification, the 2-D multiphase Poiseuille flow between two parallel plates has been simulated in some studies (Shakibaeinia and Jin, 2012; Duan et al., 2017). However, the 3-D verification is still absent. Considering that a variety of 3-D application researches would be involved in this paper, the multiphase Poiseuille flow in a 3-D circular tube is firstly studied in this section to further validate the capacity of inter-particles viscosity model in 3-D situations.

The numerical model is shown in Fig. 2. Two immiscible fluids are filled in a 3-D circular tube with the length $L = 2$ m and the diameter $D =$ 1 m. The fluid of phase II is located in the center of the tube with a diameter of 0.5 m, and the other regions are the fluid of phase I. The densities of both fluids are 2 kg/m^3. The dynamic viscosity of phase I is fixed to 0.1 Pa.s, while that of phase II changes from 0.1 Pa.s to 0.0125 Pa.s, corresponding the viscosity ratio M changing from 1 to 8. The fluids are driven by a pressure gradient $\Delta P/L = -0.5$, with the gravity and surface tension force ignored. The left and right ends of the tube are set as periodic boundary, and the radial wall is imposed the no-slip boundary condition. The analytical velocity field can be calculated by:

$$\begin{cases} u(r) = \frac{1}{2}\frac{dp}{dx}\frac{1}{\mu_1}\left(r^2 - {R_1}^2\right) R_2 < r \le R_1 \\ u(r) = \frac{1}{2}\frac{dp}{dx}\left(\frac{1}{\mu_1}r^2 - \frac{1}{\mu_2}{R_1}^2\right) + \frac{1}{2}\frac{dp}{dx}\left(\frac{1}{\mu_2} - \frac{1}{\mu_1}\right){R_2}^2 0 < r \le R_2 \end{cases} \quad (27)$$

where R_1 and R_2 are the radiuses of the circular tube and the inner fluid, respectively, and r is the radius at the position of the target particle.

Fig. 3 compares the velocity profiles calculated by multiphase MPS method and the analytical solutions with different inter-particle viscosities for $M = 4$. As it can be seen, the best agreement is obtained with the harmonic mean of viscosities while the maximum velocity at the tube center is slightly underestimated with the arithmetic mean of viscosities, similar with the conclusion of 2-D tests (Shakibaeinia and Jin, 2012). In addition, when adopting $\mu_{ij}=\mu_j$ or $\mu_{ij}=\mu_j$, the velocity profile would be greatly overestimated or underestimated compared with the analytical result.

Fig. 4 presents the velocity profiles with different viscosity ratios obtained by using the harmonic mean of viscosities, from which a fair good agreement between the numerical and analytical results is observed. Moreover, the MPS snapshots of multiphase Poiseuille flows

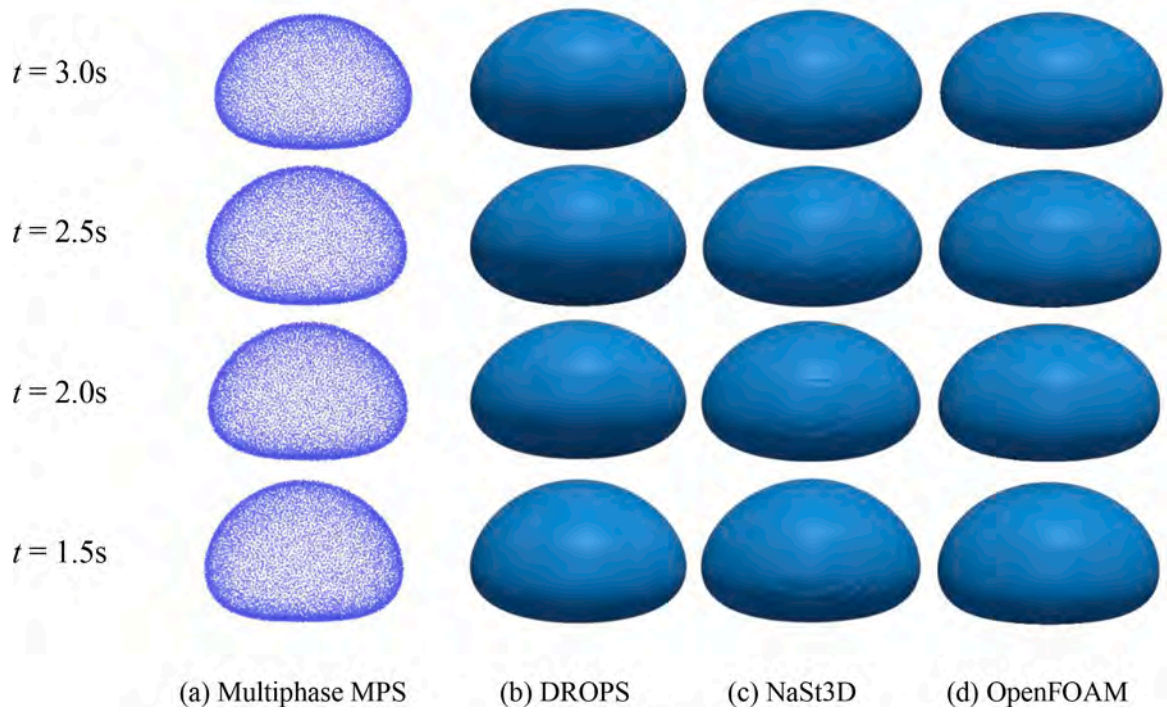

Fig. 21. Shapes of 3-D bubble captured by different methods.

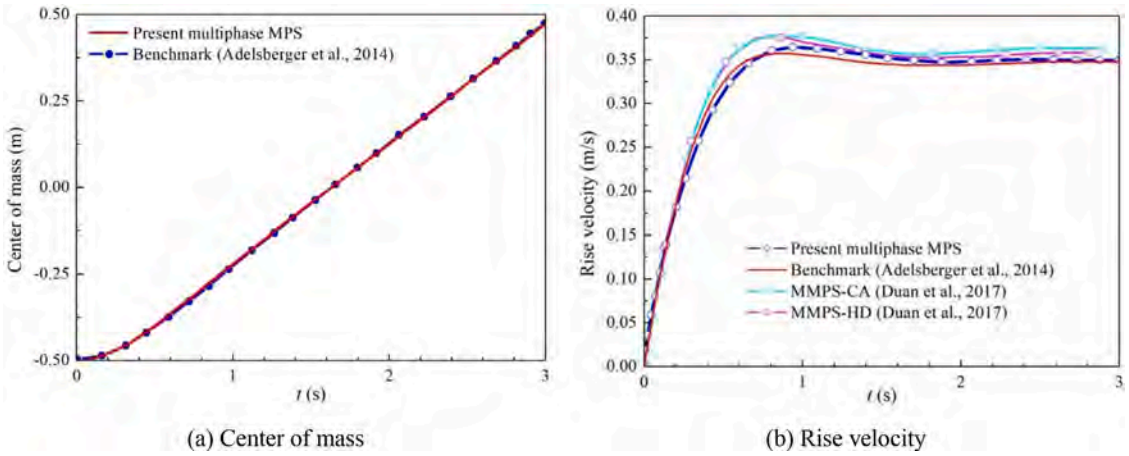

Fig. 22. Quantitative results obtained by multiphase MPS method in 3-D bubble rising and comparison with benchmark results and other numerical results.

are shown in Fig. 5. Being consistent with actual physical phenomena, the motions of two fluids become obviously differentiated as the viscosity ratio increases. In summary, it can be considered that the present multiphase MPS method is able to realize the accurate calculation of viscous force in both 2-D and 3-D cases by using the inter-particle viscosity with the form of harmonic mean.

4.2. 2-D/3-D rayleigh-taylor instability

Rayleigh-Taylor instability (RTI) is an extensively observed fingering instability in which a heavier fluid is accelerated toward a lighter fluid under the gravity effects. In this section, the RTI problem shown in Fig. 6 would be simulated by the present multiphase MPS method, which is also studied by Shakibaeinia and Jin (2012). Two immiscible fluids with different densities are placed in a rectangular container with the dimension of 0.5 m (width) × 1 m (height). The heavier fluid is located at the upper layer with the density $\rho_h = 3000$ kg/m^3, while the lighter fluid is located at the lower layer with the density $\rho_l = 1000$ kg/m^3. The kinematic viscosities of both fluids are 0.01 m^2/s and the surface tension coefficient is 0.1 N/m. The gravity acceleration is set to be $g = 10$ m/s^2 and points downwards. No-slip condition is imposed to all walls. In order to trigger the occurrence of RTI, an initial cosinoidal disturbance with the amplitude $\eta = 0.025$ m and the wave-length $\lambda = 0.5$ m is imposed on the initial interface. To test the convergence of the present method, three different particle distances are respectively adopted, including $dp = 0.002$ m, 0.003 m, and 0.004 m (Fig. 7).

Fig. 2 shows the snapshots of Rayleigh-Taylor instability at several typical instants simulated by multiphase MPS method with $dp = 0.002$ m. As it can be observed, the complex interface is clearly captured, and the calculated velocity and pressure field keep smooth. With the continuous invading of the lower fluid into the upper fluid, the initially slight disturbance grows fast and a bubble-shape interface is formed at $(\lambda/g)^{-1/2} = 2.2$. Then, the interface deforms into a mush-room shape at $t(\lambda/g)^{-1/2} = 3.3$ and becomes more complicated at $t(\lambda/g)^{-1/2} = 4.4$. From

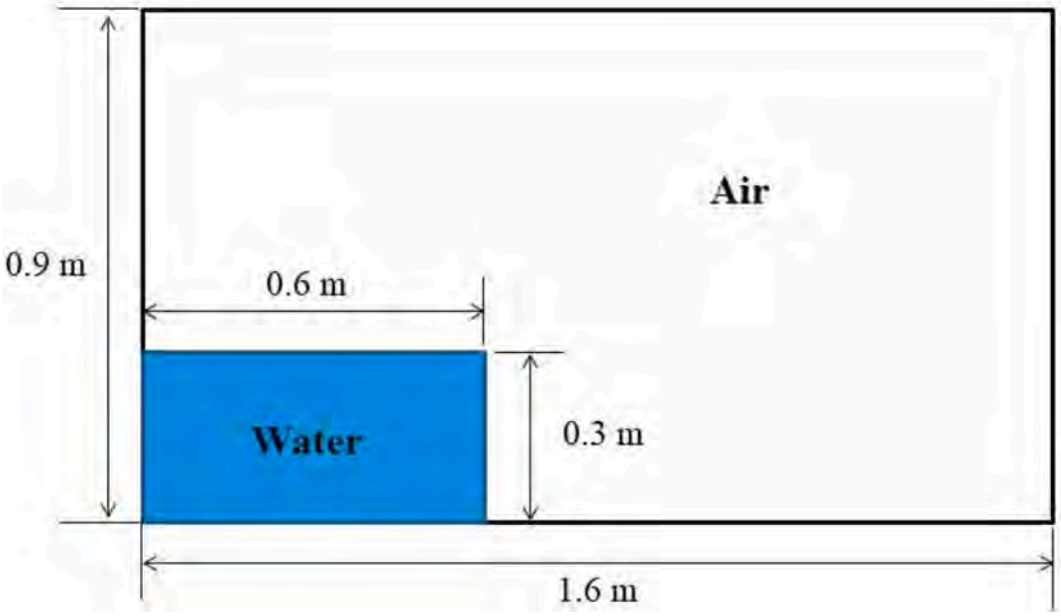

Fig. 23. Schematic diagram of 2-D dam-break flow.

the y-velocity field, it can be seen that the lighter and heavier fluids move with an opposite y-velocity under the action of initial disturbance and gravity, and with the development of RTI, the fluid movement is gradually accelerated, leading to the formation of multiple vortex structures. Meanwhile, due to the increase of mixing degree of two fluids, the pressure gradient with the depth is reduced near the interface.

Fig. 8 and Fig. 9 present the shape of phase interface in RTI at $t(\lambda/g)^{-1/2} = 4.4$ and the time evolution of maximum interfacial displacement, respectively, which are compared with the MPS and VOF results provided by Shakibaeinia and Jin (2012). It can be noted that the main characteristics of the interface captured by different methods show a good agreement, and the result of the present multiphase MPS method is closer to the VOF result. Some local differences may be caused by the different values of surface tension coefficient, which is not given in literature. Similarly, the maximum interfacial displacement calculated by different methods is in good agreement, and the penetration depth between fluids shows an exponential growth in the early stage, a linear growth in the middle stage, and a gradual deceleration in the later stage. In addition, the simulation results with different particle distance are consistent, verifying the convergence of the proposed method.

In order to verify the performance of multiphase MPS method in 3-D interfacial flows, the 3-D RTI problem shown in Fig. 10 is further simulated. The geometric size of the 3-D container is 0.5 $m \times 0.5\ m \times 2$ m (length $\times$ width $\times$ height), and the densities of the upper and lower fluids are 3000 kg/m^3 and 1000 kg/m^3, respectively. The viscosity of both fluids is 8×10^{-3} Pa.s and the gravity acceleration is $g = 9.8$ m/s^2. All tank walls are set as free-slip boundary. The particle distance is 0.01 m, thus the total number of particles reached to 845,397. The initial shape of interface is given as:

$$y = \pm(0.05\cos(4\pi x) + 0.05cos(4\pi x)) \tag{28}$$

Where the symbols (+) or (-) correspond to the convex or concave disturbance, respectively.

Fig. 11 shows the evolutions of phase interface in the 3-D RTI problems. As it can be observed, before $t = 0.5$ s, the upward and downward deformations of the interfaces caused by different disturbances are similar, and the shape of interface is relatively not complicated. However, when the mushroom structure appears at $t = 0.5$ s, the interface deformations in two cases become slightly different. Specially, the mushroom structure is inclined to a cap shape in the convex case, while it shows a spherical shape in the concave case. Moreover, the penetration rate between the upper and lower fluids is faster in the concave case, thus the interface is able to firstly impacts on the lower wall at $t = 1.1$ s.

Fig. 12 shows the cross-sectional views of phase interface in the 3-D RTI problem with a convex initial disturbance at three vertical planes, including $x = -0.25$, $x = 0$, and $x = y$. As it can be seen, the interface shapes in the $x = -0.25$ and $x = 0$ planes are similar with the results of above 2-D RTI simulation. However, the interface shape in the $x = y$ plane becomes quite different where the two-layer roll-up phenomenon can be observed. In general, the results are in qualitative agreement with the mesh-based computations of Li et al. (1996), He et al. (1999), and Lee and Kim (2013).

Benefitting from the high stability of IMPS method, the developed multiphase MPS method is able to reproduce the long-term evolution of 3-D RTI and the simulation results are shown in Fig. 13. After the contact between the phase interface and the upper or lower wall, the two fluids are mixed violently. Subsequently, the fluid particles began to move under the action of buoyancy and finally at $t = 30$ s, the flow field reached a completely stable state that the heavier fluid is all located in the lower layer while the lighter fluid is all located in the upper layer. The successful simulation of the long-term evolution process shows that the present multiphase MPS method is not only capable for capturing the phase interface deforming from a simple state to a complex state, but also can be applied to the opposite process, without numerical instability induced by the violent mixing of different fluid particles.

In the last part of this section, the multiphase MPS method is applied to simulate the multi-mode 3-D RTI problem shown in Fig. 14. The physical properties of fluids and the initial shape of interface keep identical with the above single-mode 3-D RTI problem with a convex disturbance, but the calculation domain is expanded to $1\ m \times 1\ m \times 2$ m (length $\times$ width $\times$ height). Therefore, the total number of particles in this case increases to about 2.72 million. Fig. 15 shows the evolution of phase interface obtained by the multiphase MPS method. Although the interface becomes quite complex in this case, it still can be accurately captured and the long-time evolution process is well reproduced, validating the applicability of the present method in the numerical simulation of large-scale 3-D interfacial flows.

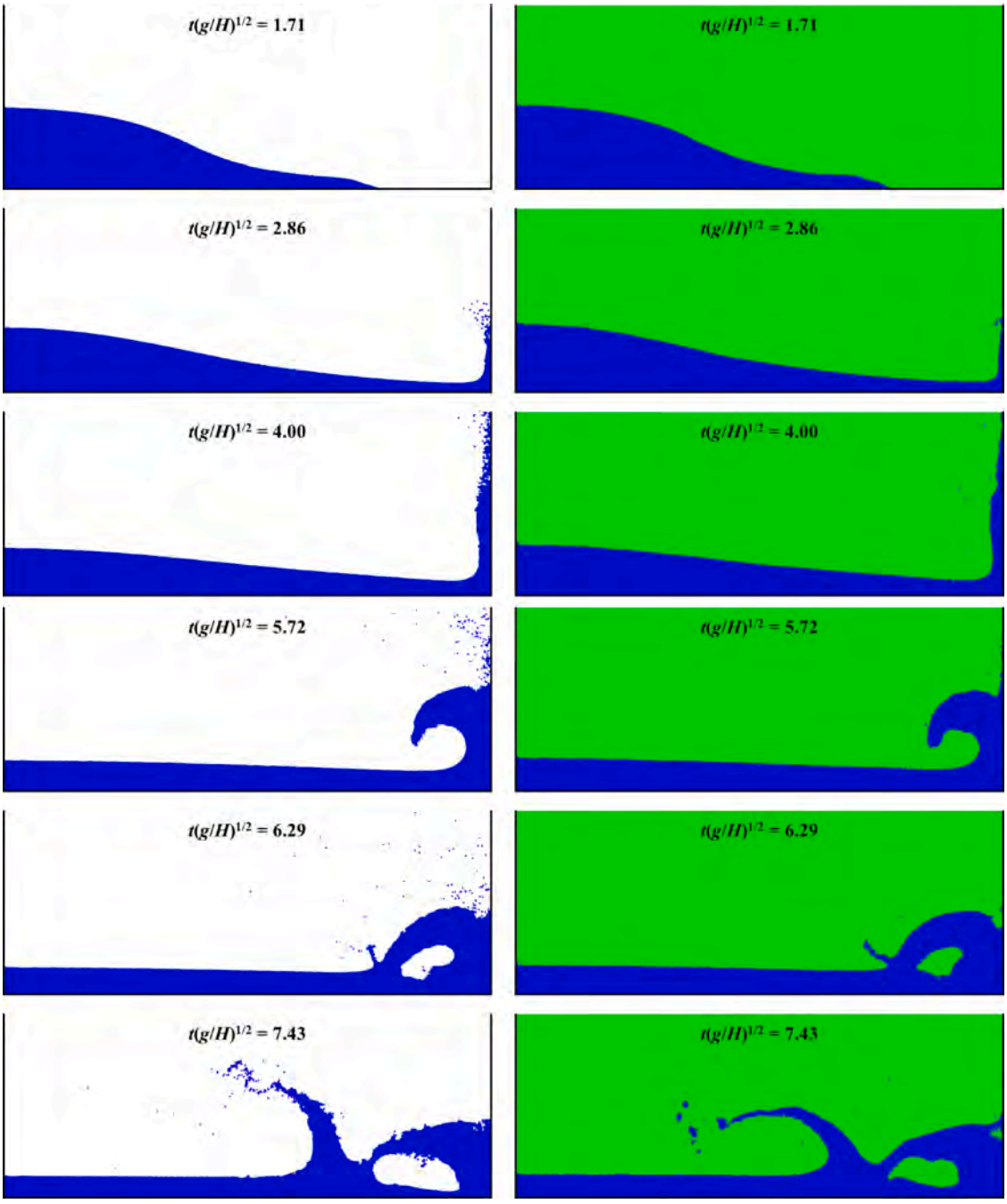

Fig. 24. Snapshots of dam-break flow (left: IMPS method; right: multiphase MPS method).

4.3. 2-D/3-D bubble rising

Bubbly flow is one of the most widely existed interfacial flow phenomena in nature. In this section, the 2-D/3-D single bubble rising are studied by using the multiphase MPS method. The initial configurations keep identical with the 2-D benchmark study of Hysing et al. (2008) and the 3-D benchmark study of Adelsberger et al. (2014), as shown in Fig. 16. In 2-D case, a circular bubble with the diameter $d = 0.5$ m is initially centered at (0.5, 0.5) in a 1×2 rectangular container. No-slip boundary condition is imposed on the top and bottom walls, while the free-slip boundary condition is imposed on the vertical sidewalls. In 3-D case, a sphere bubble with the diameter $d = 0.5$ m is initially centered at (0.5, 0.5, 0.5) in the $1 \times 1 \times 2$ cuboid container and all tank walls are set as no-slip boundary. The same physical property of fluids is adopted in 2-D and 3-D cases, being consistent with the "case 1″ of the benchmark study, in which both the density and viscosity ratios are 10:1. The Reynolds number (*Re*) representing the ratio of inertial to viscous effects is equal to 35, and the Bond number (*Bo*, also known as Eotvos number) representing the ratio of gravitational forces to surface tension effects is equal to 10.

Fig. 17 presents the simulation results of bubble rising obtained by multiphase MPS method at several typical instants. Due to its density difference with the surrounding liquid, the bubble rises rapidly from its initial position under the action of buoyancy, and the interface suffers from large deformation in the rising process. Especially, the interface at the bottom of the bubble turns into a flat shape, and is slightly convex at $t = 2$ s. Then, the bubble gradually recovers to a circular shape due to the surface tension effects, and at the end of simulation, i.e., $t = 3$ s, the bubble locates in an elliptical shape. In general, the complex interface is well captured by the multiphase MPS method, and the calculated

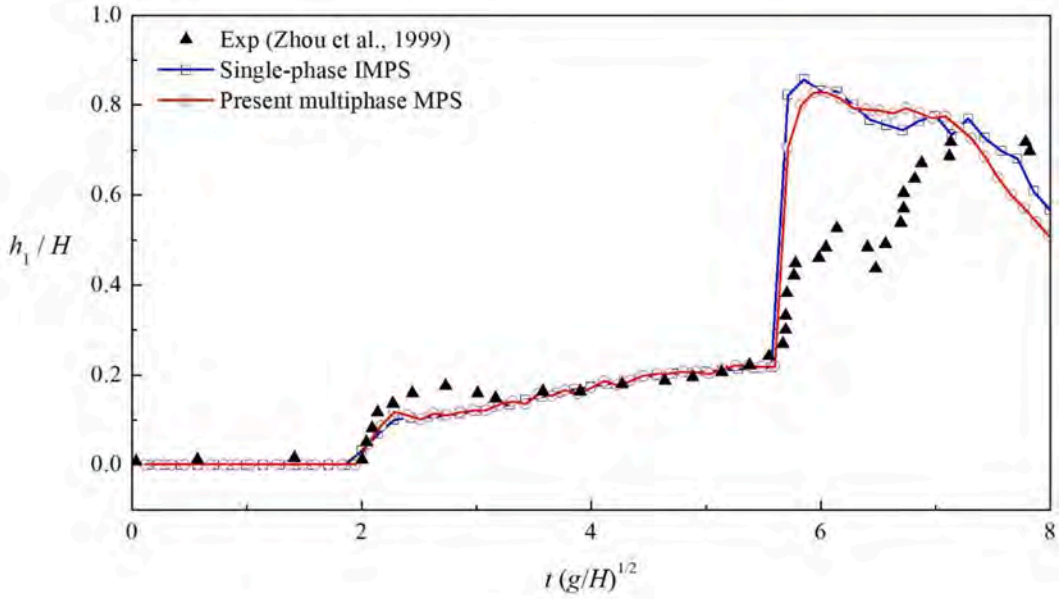

(a) $x/H = 0.825$

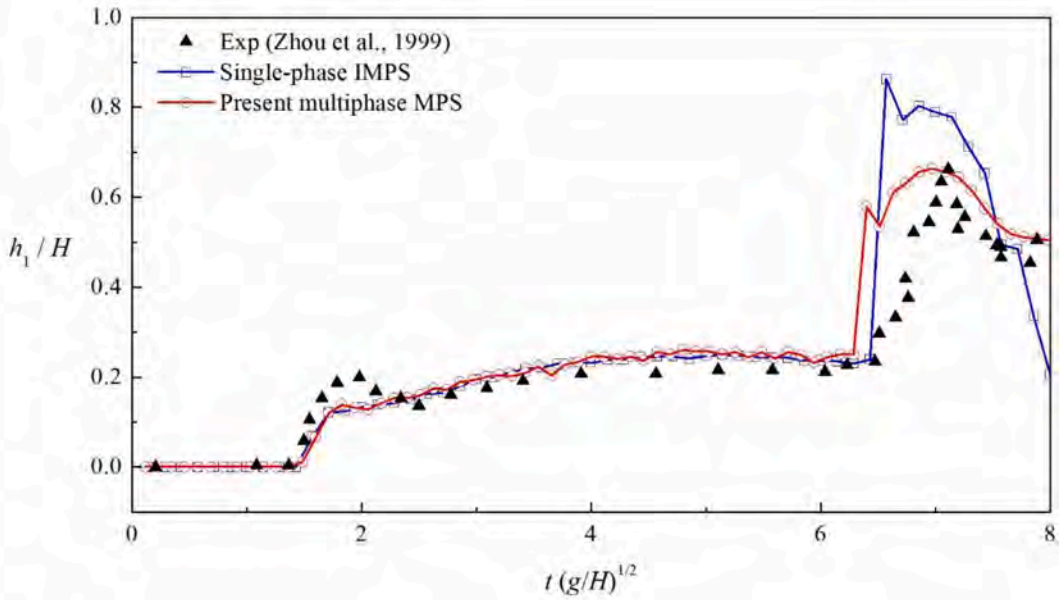

(a) $x/H = 1.654$

Fig. 25. Time evolutions of water heights at different locations.

velocity field and pressure field keep quite smooth.

Fig. 18 compares the final bubble shape at $t = 3$ s predicted by multiphase MPS method with the benchmark results, from which a good agreement is observed. To further analyze the motion characteristics of bubble, Fig. 19 shows the calculated center of mass and rise velocity of the bubble in the rising process. It can be seen that the velocity of bubble increases rapidly in the early stage, and a peak velocity is observed at $t = 1$ s due to the resistance force of the surrounding fluid. Subsequently, the bubble velocity begins to decrease and finally reached a stable value. The results of multiphase MPS method are in good agreement with the benchmark results, and the fluctuations of bubble velocity observed in some other particle methods are effectively avoided, verifying the high stability of the present method.

Fig. 20 shows the time evolution of the 3-D bubble shape simulated by multiphase MPS method. As it can be seen, the bubble gradually becomes ellipsoid in the rising process, but its deformation is smaller than that of the 2-D rising bubble studied above. After $t = 2.0$ s, the bubble shape keeps almost stable. In Fig. 21, the shapes of 3-D bubble obtained at several typical time instants are compared with the benchmark results by three different mesh-based solvers, including DROPS, NaSt3D and OpenFOAM (Adelsberger et al., 2014), which shows a good agreement.

From the comparison in Fig. 22, it can be seen that the center of mass calculated by the present multiphase MPS method keeps consistent with the benchmark results. Different from the 2-D case, the rise velocity of 3-D bubble did not decrease significantly after the peak value, but quickly reached a stable state. Both the developed method in this paper and the other two multiphase MPS methods proposed by Duan et al. (2017)

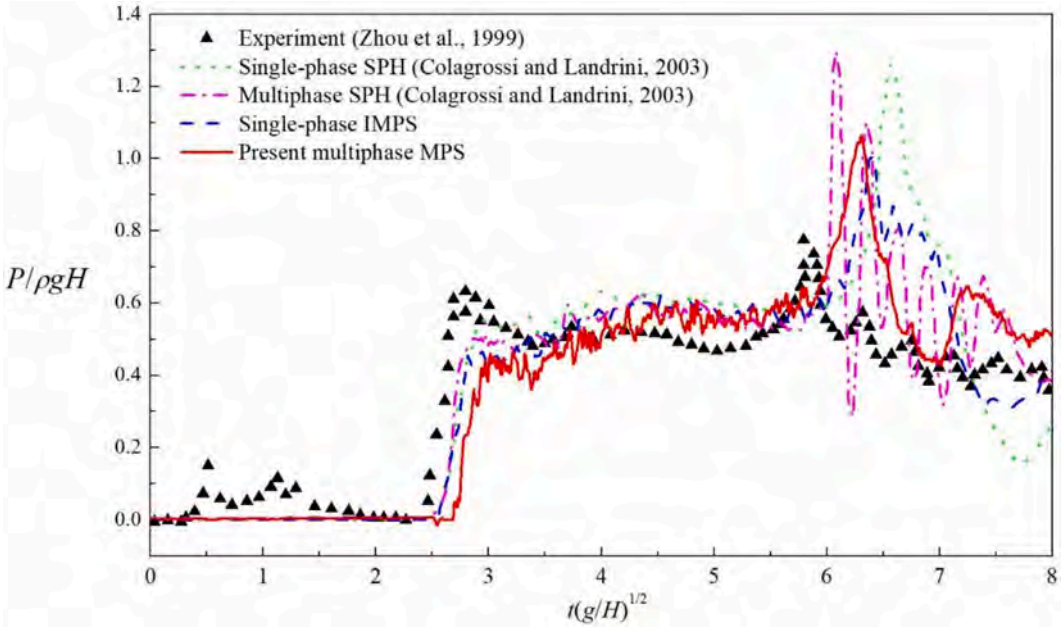

Fig. 26. Time history of impact pressures on the right wall predicted by different methods.

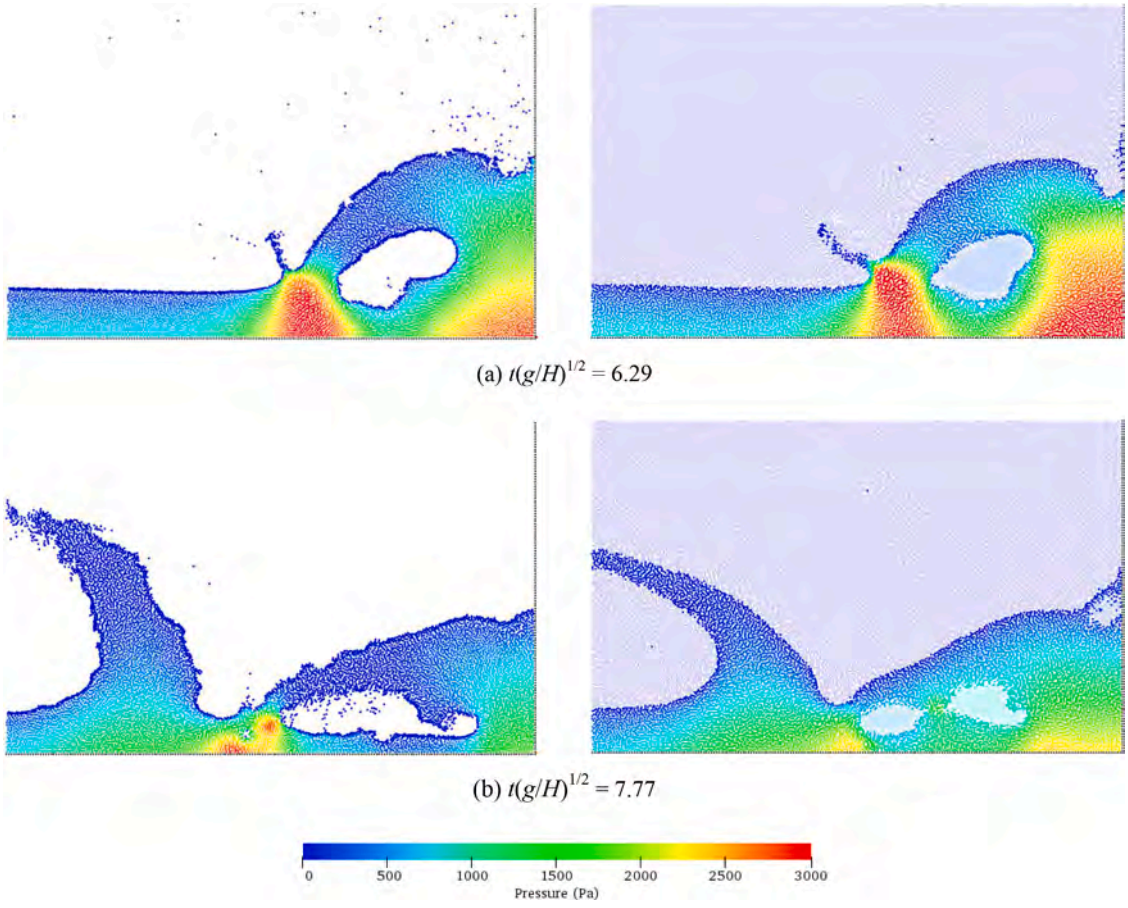

Fig. 27. Pressure fields corresponding to the second pressure peak and the collapse process. (left: IMPS method; right: multiphase MPS method).

obtain similar results with the benchmark results. There are some slight differences observed. However, considering that even the three mesh-based methods in benchmark study show different results, the accuracy of present work can be regarded as acceptable.

4.4. 2-D/3-D dam-break flow

Dam-break flow is accompanied by strong impact and nonlinear evolution of water-air interface, such as the overturning and breaking of

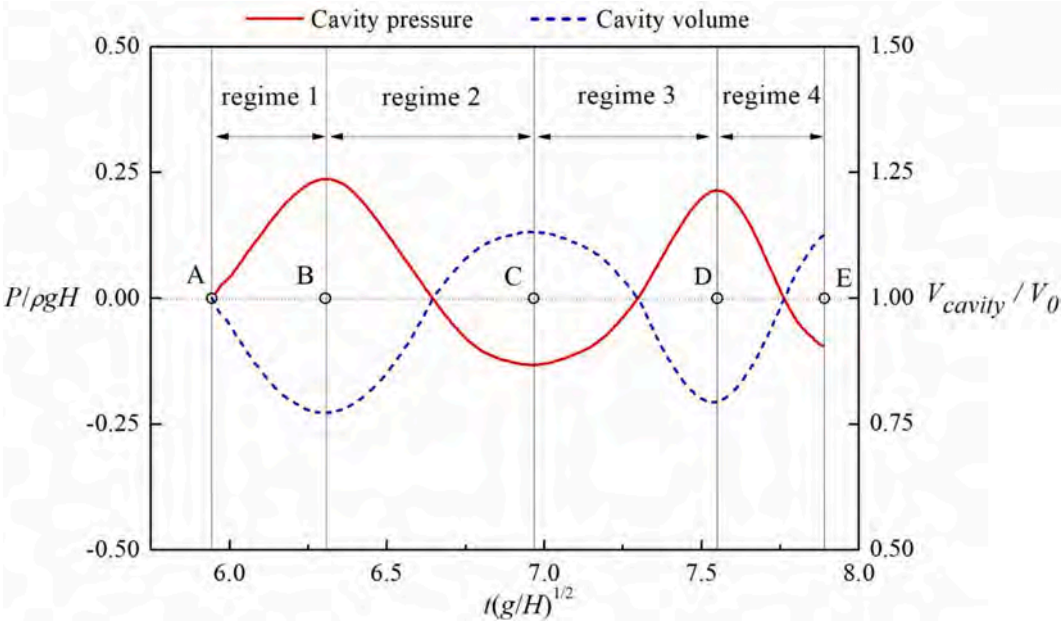

Fig. 28. Time evolutions of dimensionless pressure and volume of the air cavity. (V_0 - cavity volume at initial state).

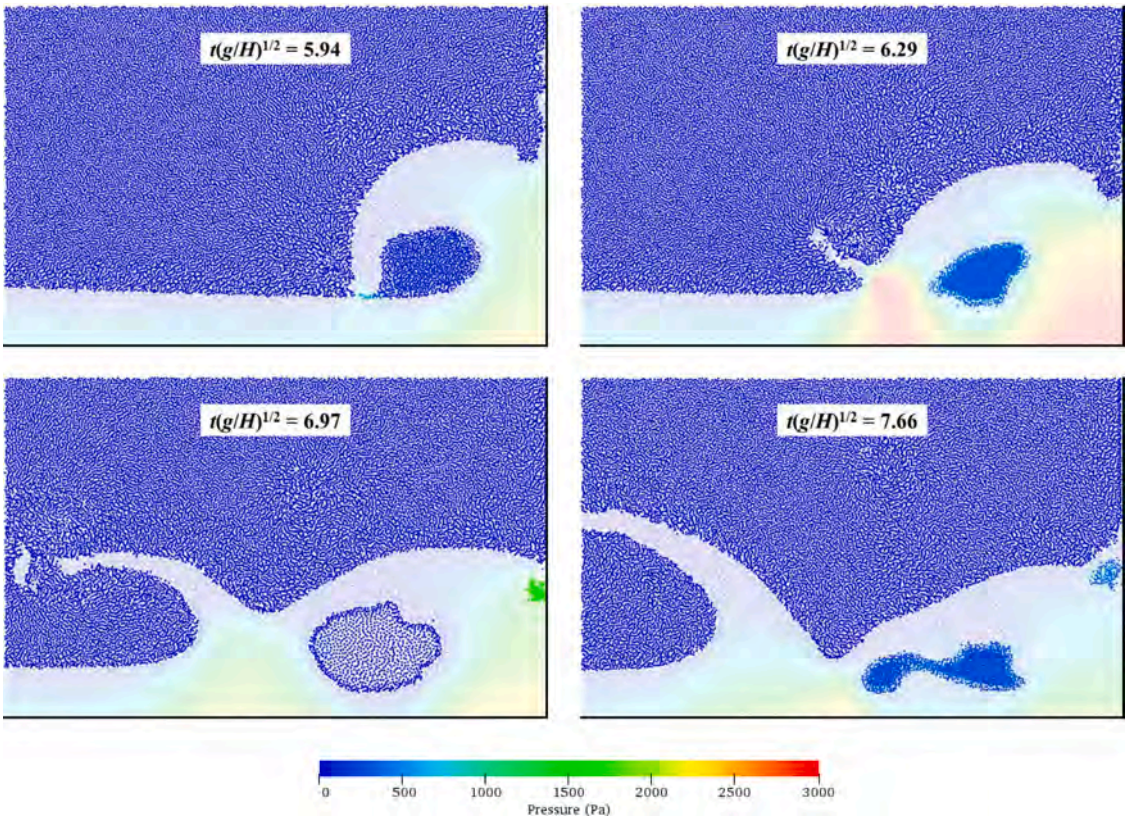

Fig. 29. Shape and pressure of the air cavity.

waves, which is quite suitable for the application of MPS method. In this section, the multi-phase MPS method would be firstly employed to simulate the 2-D dam-break problem shown in Fig. 23. At the initial moment, the water occupies an area of 0.6 m (width) × 0.3 m (height) on the lower-left corner of the rectangular container, with the remaining parts filled with air. The real viscosities of water and air are adopted, and the densities of water and air are 1000 kg/m^3 and 1.29 kg/m^3, respectively, thus the density ratio is more than 800 in this case.

Fig. 24 shows the snapshots of dam-break flows simulated by IMPS and multiphase MPS methods, respectively. In general, the typical hydrodynamic phenomena induced by dam-break flow can be captured by both methods, including the strong impact, wave breaking and water jet, etc. However, some discrepancies are generated due to the different treatments of air phase. Firstly, the water splashing is more significant in the single-phase simulation. The reason is that the air region is regarded as a vacuum by IMPS method, resulting in less resistance for fluid

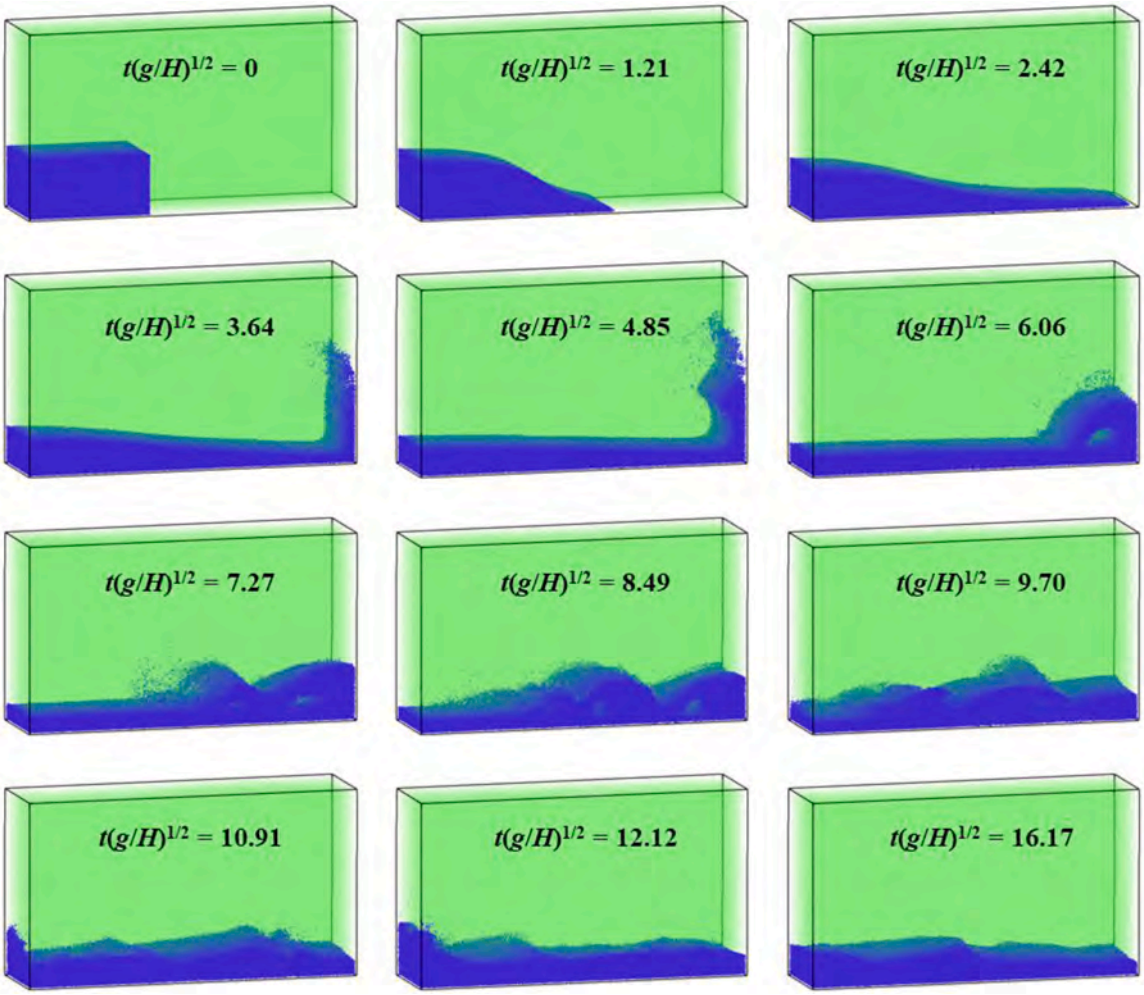

Fig. 30. Evolution of 3-D dam break flow simulated by multiphase MPS method.

particles to escape from the free surface. Meanwhile, the surface tension effects considered only by the multiphase MPS method also provide additional energy for the fluid particles to remain inside the water body.

Another difference appears after the backward plunging water front impacts the free surface. Due to the cushion effect of air, the height of water jet in the multiphase simulation is much lower than that in the single-phase simulation, which keeps consistent with the SPH results of Colagrossi and Landrini (2003). Meanwhile, a mass of air is trapped and formed an air cavity. Due to the neglection of air phase, the shape of cavity in the single-phase simulation is completely dependent on the movement of water phase, thus increases rapidly from $t(g/H)^{1/2} = 6.29$ to 7.43. In the multiphase simulation, the deformation of cavity would be limited by the compressibility of the entrapped air particles, hence the change of cavity volume is relatively smaller.

Fig. 25 presents the time evolution of water heights at locations of $x/H = 0.825$ and $x/H = 1.653$ from the right wall, respectively. In general, the variation trends obtained by two methods show a good agreement with the experimental results (Zhou et al., 1999). However, the measuring equipment used in the experiments are sensitive to the wetted portion of the wire, thus the height of air cavity is not included and the measured water height is lower than the numerical results, especially at $x/H = 0.825$ where the main part of cavity is located. The calculation results of single-phase and multiphase methods keep basically consistent at $x/H = 0.825$, but the water height at $x/H = 1.653$ is much larger in the single-phase simulation at $t(g/H)^{1/2} \cong 6.4$, caused by the more severe water jet phenomenon observed in Fig. 24.

Fig. 26 shows time history of impact pressures predicted by different methods. The pressure probe is located on the right wall and $0.267H$ above the bottom. As it can be seen, the pressure curves obtained by both IMPS and multiphase MPS methods show some difference from the experimental results. Meanwhile, this difference is also observed in the SPH result of Colagrossi and Landrini (2003). In fact, Zhou et al. (1999) has reported difficulties to achieve repeatability of the measurements in experiment and no conclusive statement can be made. Other than that, we should note that all numerical methods are able to give reliable predictions of the pressure tendencies. Firstly, the impact of the water front against the right wall is accompanied by a sudden pressure rise at $t(g/H)^{1/2} \cong 2.4$, which is well captured by both IMPS and multiphase MPS methods. Then, a second pressure peak is induced by the backward plunging water front. For this pressure peak, the multiphase MPS result is a bit of earlier and larger than the single-phase MPS result, which is also identified in the comparison between the single-phase and multiphase SPH results. Compared with the multiphase SPH results, the present multiphase MPS result suffers from less fluctuations after the second pressure peak. The reason is that in the multiphase SPH method, both the air phase and water phase are regarded as compressible. Therefore, the volume of water phase fluctuates with the air phase during the impacting process, leading to the pressure oscillation. In the present multiphase MPS method, the compressible-incompressible model is adopted and the water phase is treated as fully incompressible, thus the pressure field is kept stable.

In the dam-break flow, the air cavity has an important influence on the accurate calculation of impact pressure. Fig. 27 shows the pressure fields corresponding to the second pressure peak and the collapse

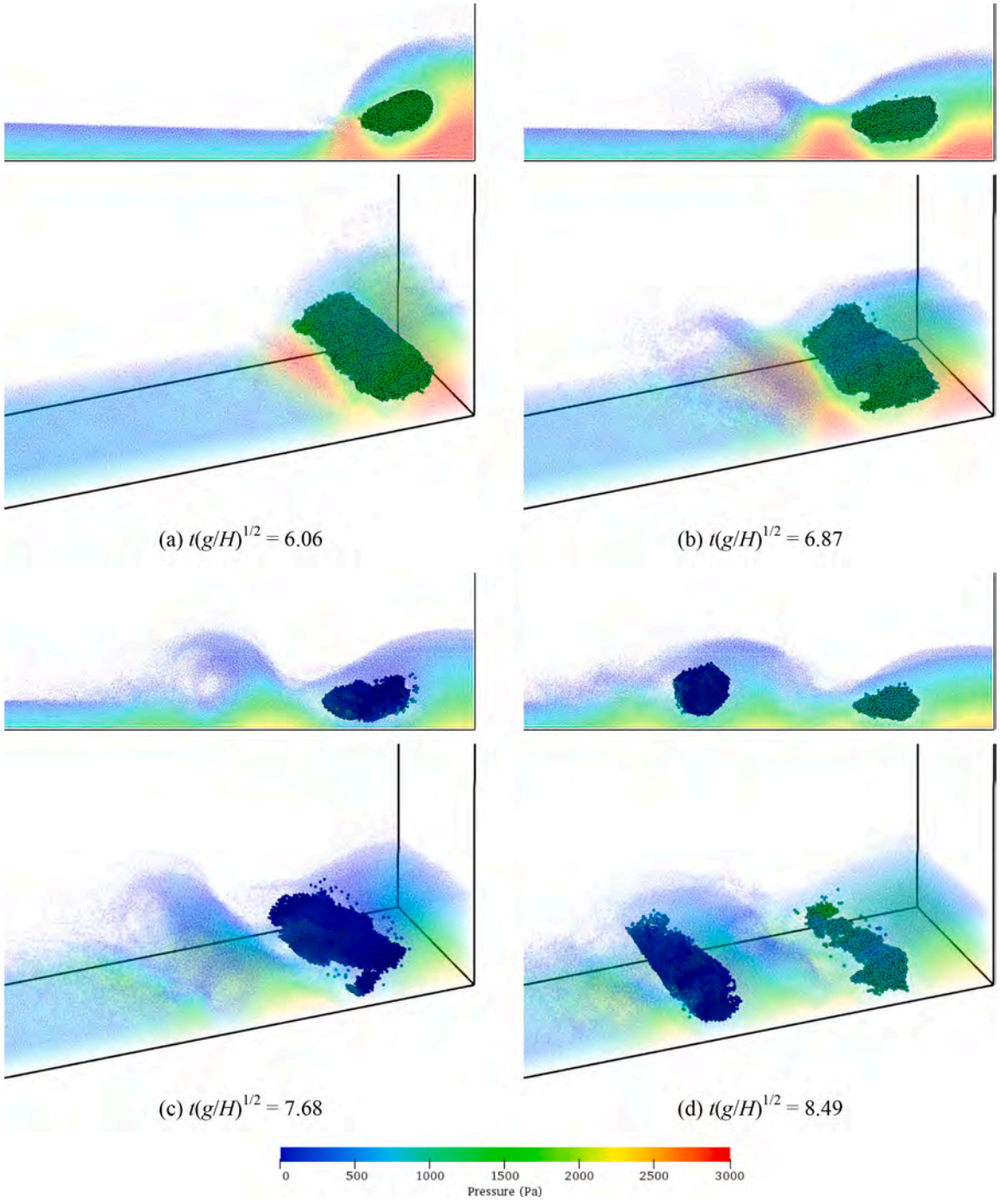

Fig. 31. Phenomenon of air entrapment in 3-D dam-break flow.

process of cavity, respectively. Note that, the air particles are set to be transparent. Firstly, it can be seen that in the single-phase simulation, the water particles around the air cavity are misjudged as free surface particles due to the truncation of the influence domain, and are wrongly given zero pressure, resulting in an inaccurate pressure field. Meanwhile, the water particles above the air cavity fall down freely at $t(g/H)^{1/2} = 7.77$ due to the lack of particles below. In contrast, this problem can be naturally avoided by the multiphase MPS method with the consideration of air particles. Besides, the aggregation of zero-pressure free surface particles occurs in the single-phase simulation, while the particle distribution keeps uniform in the multiphase simulation because the pressures of free surface particles are calculated by solving the PPE.

From the phase field at $t(g/H)^{1/2} = 6.29$, it can be observed that the impacting of backward plunging water front on free surface leads to the formation of air cavity and the rise of pressure inside the cavity. The pressure rise can be quickly felt in a large water region, including the corner part where the pressure probe locates. However, the air cavity is regarded as a vacuum in the single-phase simulation, thus the impacting pressure can only be transferred through the circulatory flow around the cavity, resulting in the delay of the second pressure peak observed in Fig. 26. At $t(g/H)^{1/2} = 7.77$, the impacting process is finished and the air cavity start to collapse. Due to the extrusion caused by the falling movement of the upper water, the internal pressure of the cavity increases and further transmitted to the pressure probe, inducing another peak in the pressure curve obtained by multiphase MPS method.

In Fig. 28, the time evolutions of dimensionless pressure and volume

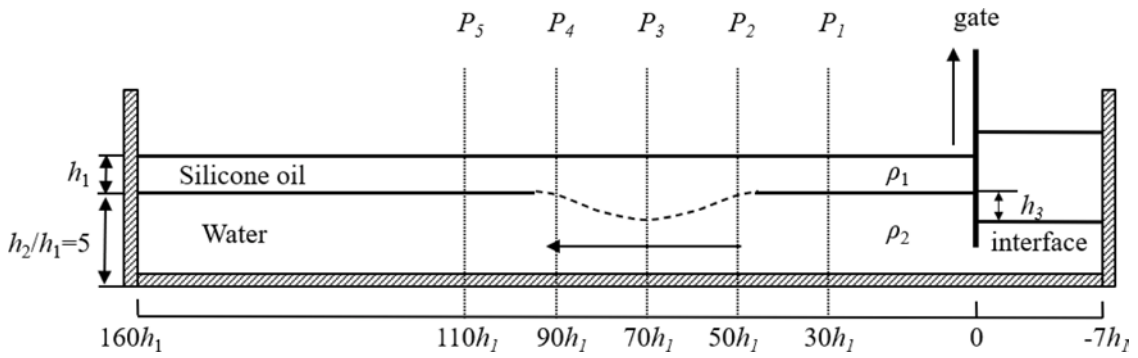

Fig. 32. Schematic diagram of 2-D internal solitary wave.

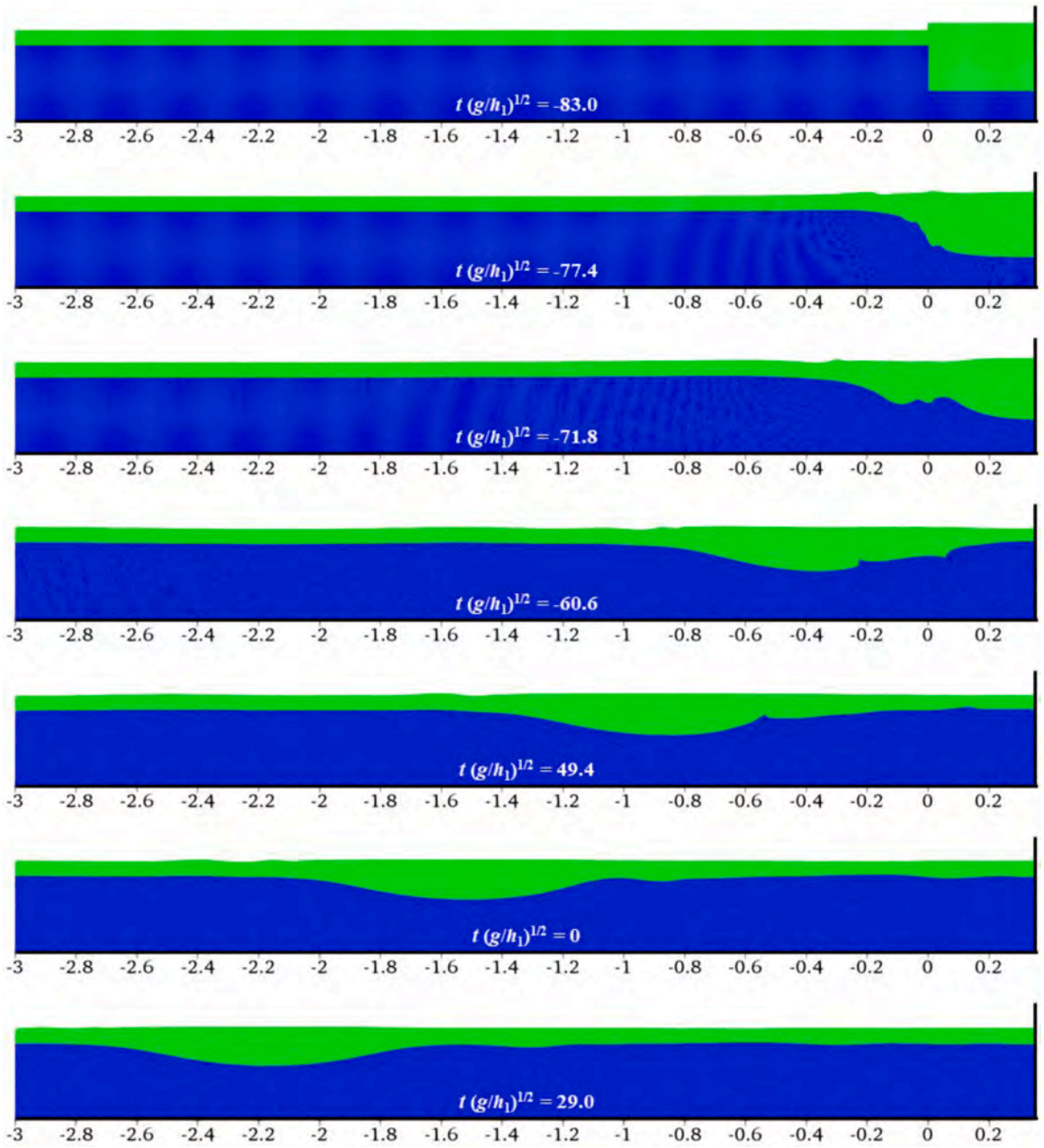

Fig. 33. Generation of internal solitary wave simulated by multiphase MPS method, dp = 0.001 m.

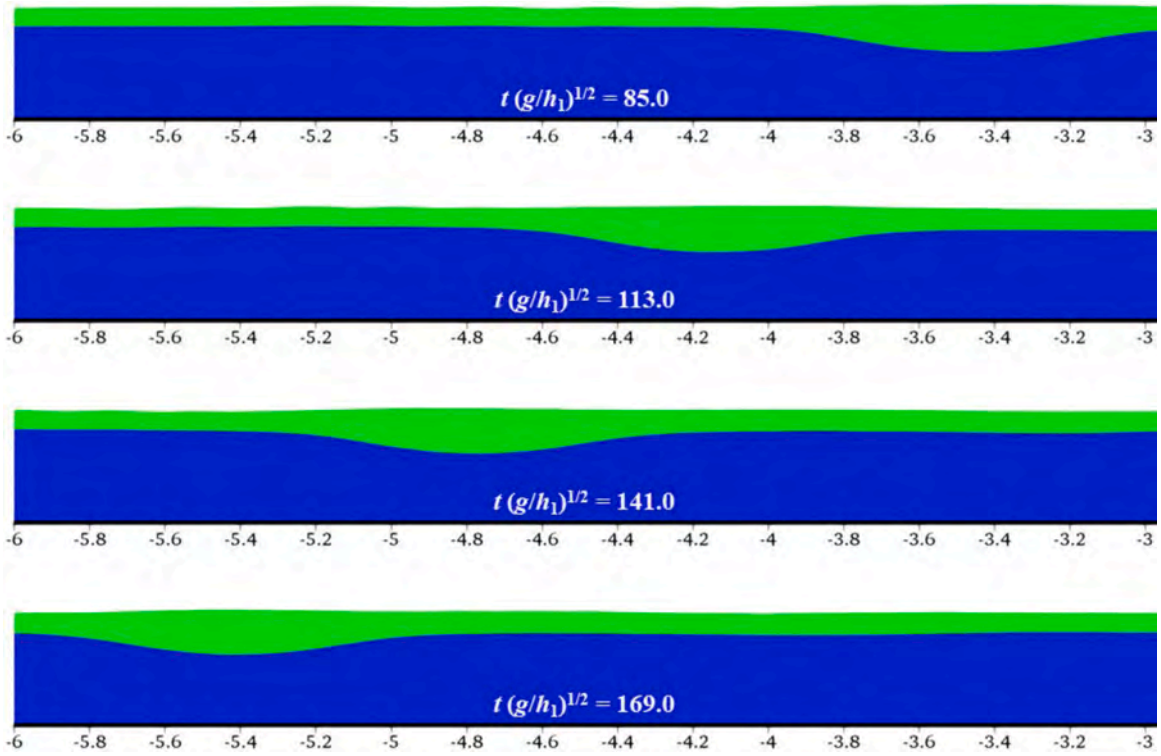

Fig. 34. Propagation of internal solitary wave in the middle section of numerical tank, dp = 0.001 m.

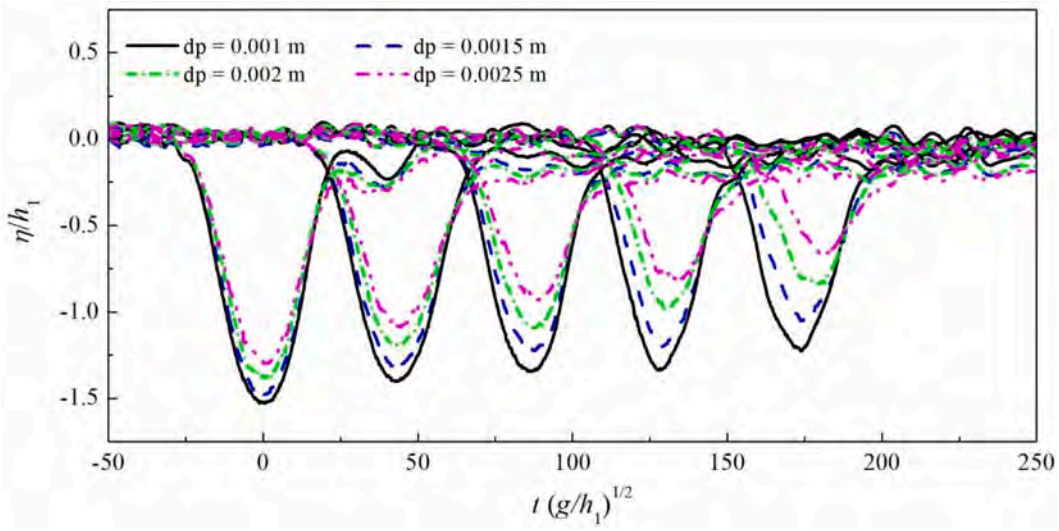

Fig. 35. Interfacial displacements at five wave probes predicted by multiphase MPS method.

of the air cavity are presented. As it can be seen, the air cavity experiences severe pressure and volume oscillations, and the variation trend of pressure and volume keeps opposite. In general, the deformation process of air cavity can be divided into four regimes. In regime 1, the air cavity is formed at $t(g/H)^{1/2} = 5.94$ and then continuously compressed due to the strong impact, leading to the increase of internal pressure. In regime 2, the impacting phenomenon becomes less violent at $t(g/H)^{1/2} = 6.29$ and the air cavity begins to expand under the influence of water movement. In regime 3, the cavity is compressed again during the collapse process, and finally, the air cavity broke up at $t(g/H)^{1/2} = 6.66$ and the trapped air started to escape in regime 4.

The shape and pressure of the air cavity at several typical time instants are presented in Fig. 29. In general, the evolutional characteristics of air cavity in different regimes are accurately captured by the present multiphase MPS method. The distribution of water particles keeps uniform throughout the entire simulation, while the distribution of air particles inside the cavity is able to become dense or sparse with the change of cavity volume, through which the effectiveness of the compressible-incompressible model employed in this paper can be validated.

In order to analyze the 3-D effects in the dam-break flow, the multiphase MPS method is further applied to the 3-D simulation of dam-break flow in this section. The 3-D numerical model is basically consistent with the 2-D model shown in Fig. 23, but the thickness of 0.45 m is considered in the third dimension of the container. Hence, the total number of particles used in this case reaches up to about two

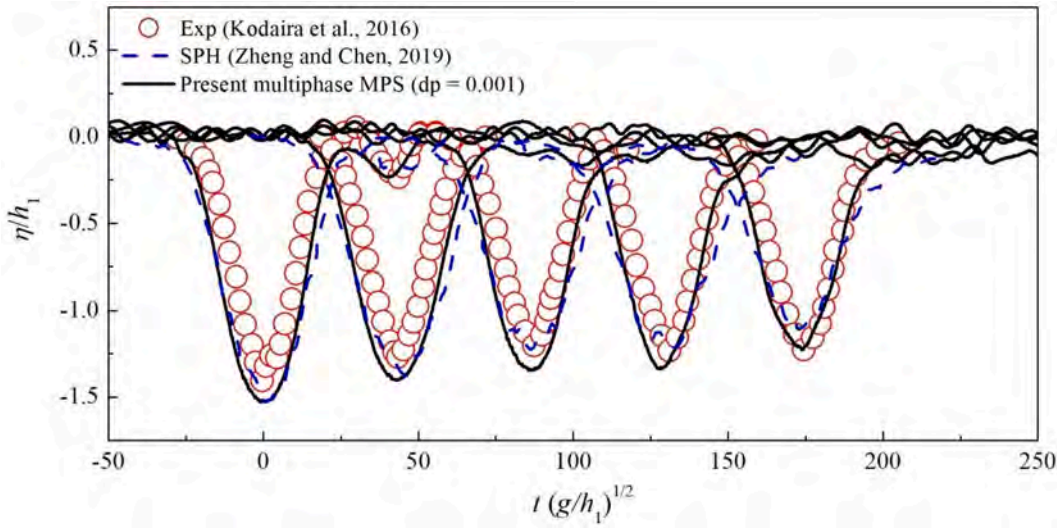

Fig. 36. Comparison of interfacial displacements between MPS, SPH, and experimental results.

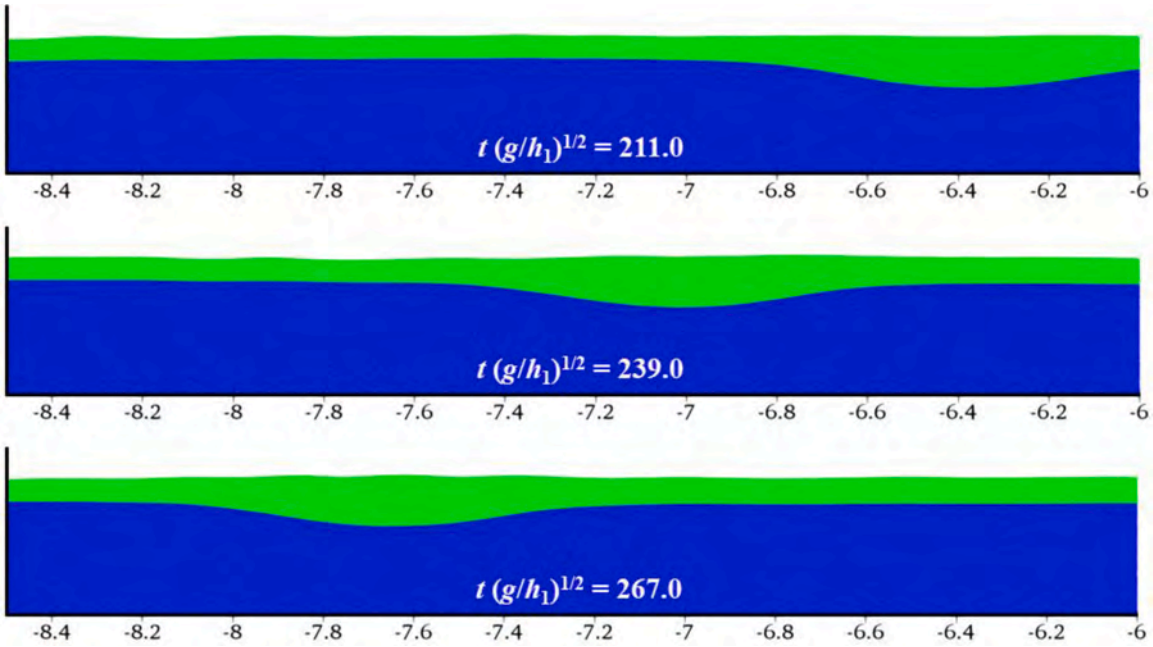

Fig. 37. Dissipation of internal solitary wave through long-distance propagation.

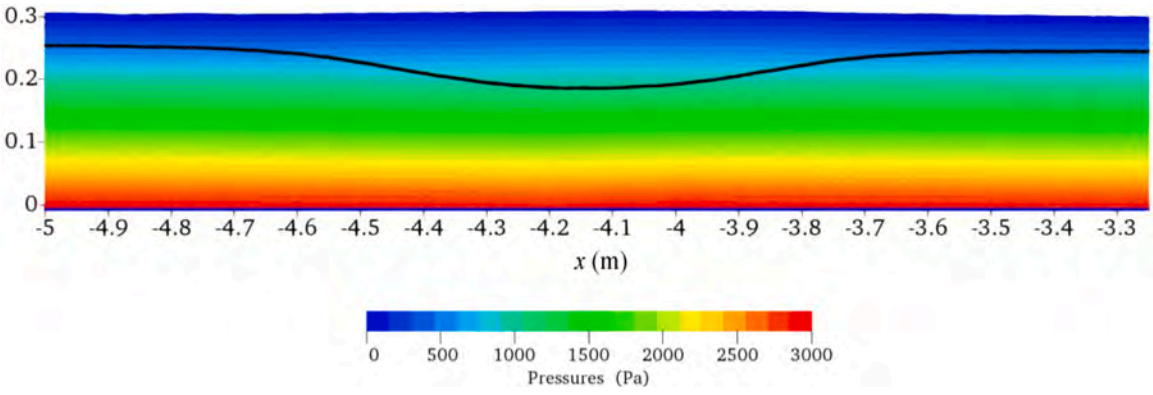

Fig. 38. Pressure field of internal solitary wave at $t(g/h_1)^{1/2} = 85$.

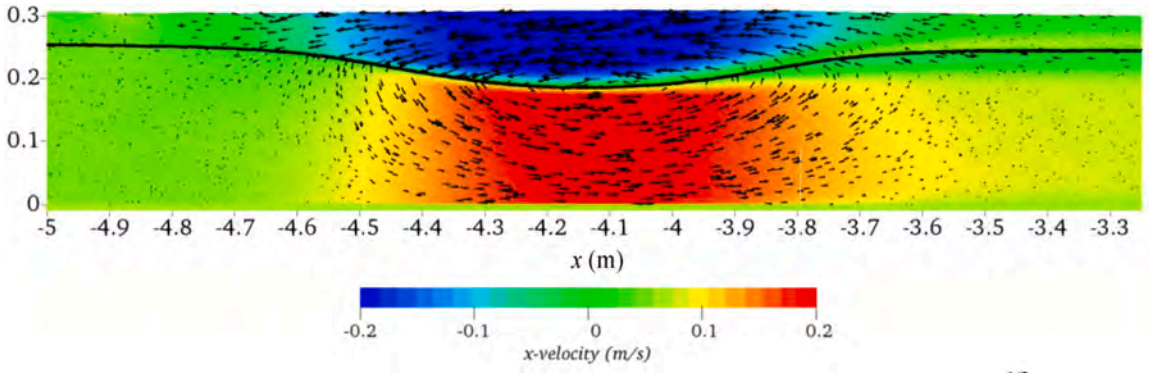

Fig. 39. x-velocity field and vector distribution of internal solitary wave at $t(g/h_1)^{1/2} = 85$.

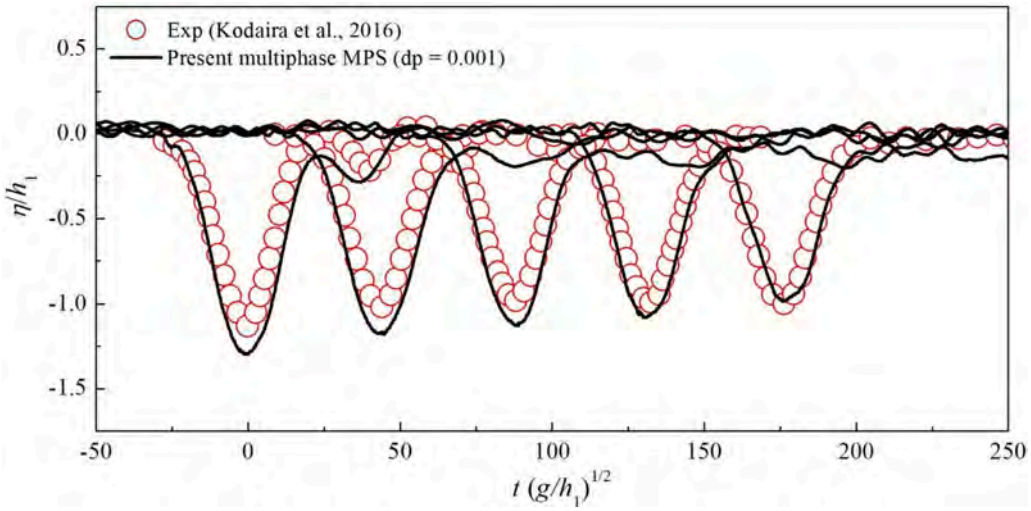

Fig. 40. Interfacial displacements of internal solitary wave, $dp = 0.001$ m, $h_3 = 0.12$ m.

million.

Fig. 30 shows the evolution of 3-D dam-break flow simulated by the present multiphase MPS method. Similar with the 2-D results, the typical hydrodynamic phenomena in dam-break flows are well reproduced. Meanwhile, the formation, deformation and collapse of 3-D air cavity is accurately simulated. From the simulation results at $t = 4.0$ s, it can be seen that the flow field gradually recovers to be stable after a long-term evolution process and the previously trapped air particles are almost all escaped, thus the different fluids reach a completely separated state again. Fig. 31 shows the phenomenon of air entrapment in 3-D dam-break flow. As it can be observed, when the 3-D air cavity is initially formed at $t(g/H)^{1/2} = 6.06$, the distribution of air particles inside the cavity keeps almost uniform along the thickness direction. However, with the continuous development of dam-break flow, the shape of cavity becomes quite complex and shows significant 3-D effects.

4.5. 2-D internal solitary wave

Internal solitary waves propagating along a density interface have been observed at many locations in the stratified oceans. As internal solitary waves propagate, they carry considerable momentum and energy, resulting in significant transient hydrodynamic loading on any offshore structures, undersea navigation vehicles and subsurface storage facilities that they may encounter. In this section, the generation and propagation of a 2-D internal solitary wave are simulated with the present multiphase MPS method. For the further comparison and verification, the selection of numerical model is based on the tank size and fluid parameters of the experiment by Kodaira et al. (2016). As illustrated in Fig. 32, the computational domain is a rectangle container filled with two immiscible fluids. The top layer is a $h_1 = 0.05$ m thick silicone oil layer with a density of 0.996×10^3 kg/m^3 and the bottom layer is a $h_2 = 0.25$ m thick water layer with a density of 0.856×10^3 kg/m^3. A vertically removable sluice gate is mounted at $x = 0$ m, which divided the wave tank into two parts. To generate the internal solitary waves, an interfacial displacement h_3 is initially set between two sides of the sluice gate, thus the free surface on the right side of the gate is slightly higher. Five wave probes are arranged at $x = 30h_1$, $50h_1$, $70h_1$, $90h_1$, $110h_1$, respectively.

Firstly, the internal solitary wave with $h_3 = 0.15$ m is simulated with an initial particles distance of 0.001 m. In Fig. 33, the consecutive snapshots during the wave generation process are presented. When the sluice gate is removed, the gravity collapse induces an internal dam-break flow and the locked lighter fluid on the right side of the gate moves forward into the ambient fluid. Meanwhile, the phase interface gradually concaves and an internal solitary wave of depression type is formed at $t(g/h_1)^{1/2} = 29$. Then, the internal solitary wave begins to propagate to the left and the waveform becomes more symmetrical. In addition, several tail waves with smaller amplitudes are generated after the main wave.

Fig. 34 shows the stable propagation process of the internal solitary wave in the middle section of numerical tank from $t(g/h_1)^{1/2} = 85$ to $t(g/h_1)^{1/2} = 169$. It can be seen that the internal solitary wave is able to propagate a quite long distance with the waveform maintained stable. There is no obvious decrease of the wave amplitude observed with the increase of propagation distance. The wave profile capture by the present multiphase MPS method is also clear and nature, demonstrating the

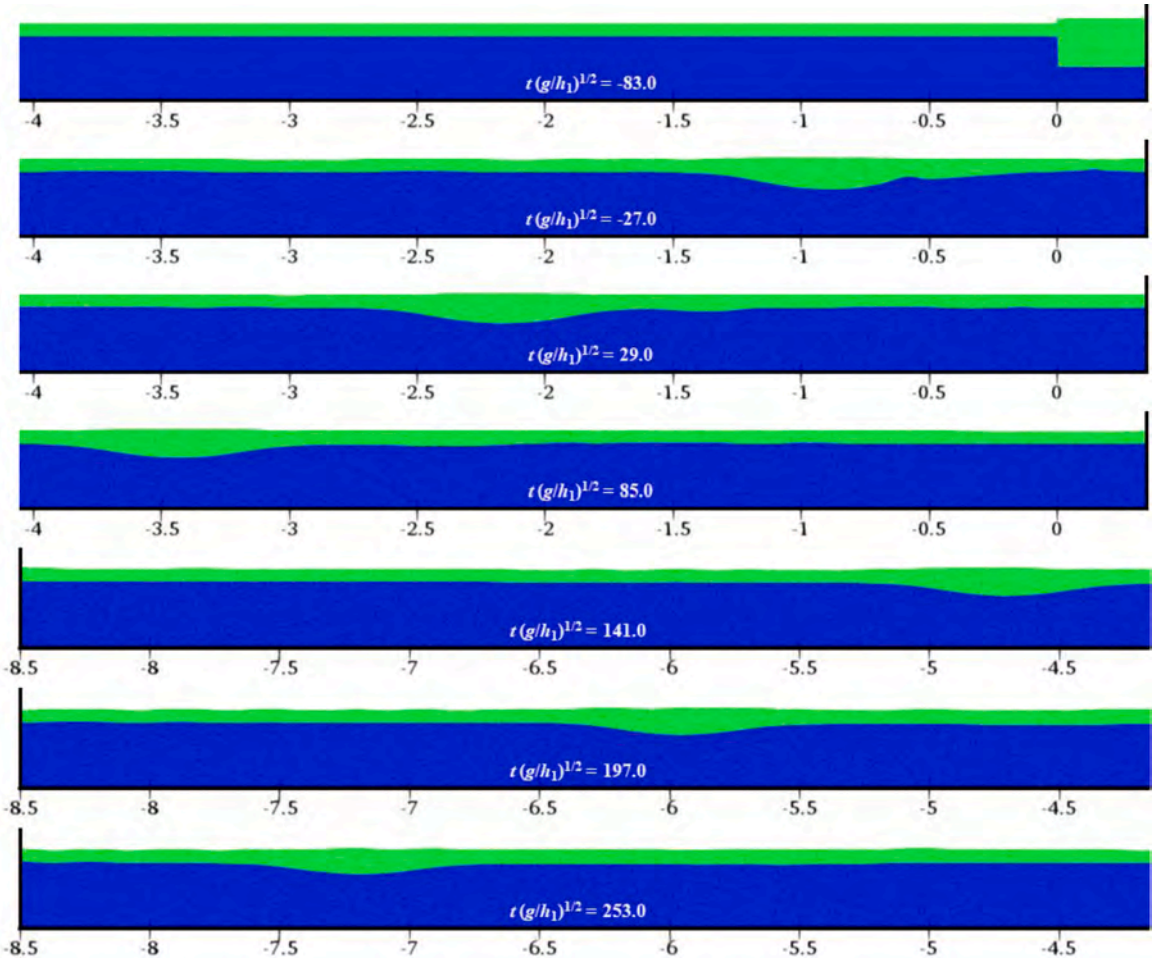

Fig. 41. Evolution of internal solitary wave, $dp = 0.001$ m, $h_3 = 0.12$ m.

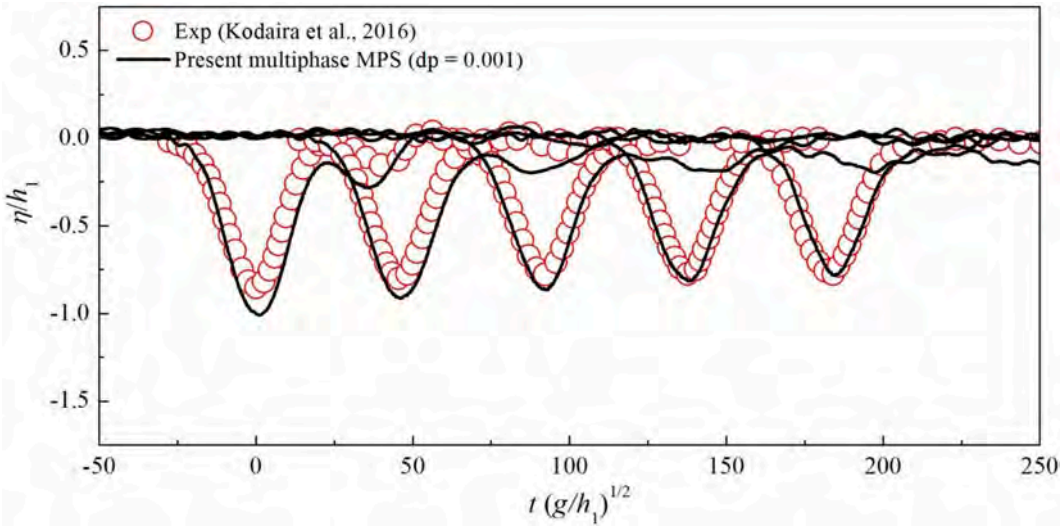

Fig. 42. Interfacial displacements of internal solitary wave, $dp = 0.001$ m, $h_3 = 0.09$ m.

advantage of the present method in interface capturing.

Fig. 35 shows the wave heights calculated with different initial particle spacings, from which we can concluded that the calculation accuracy of wave height is significantly affected by the particle resolution. When the particle spacing is 0.0025 m, the low resolution causes serious numerical diffusion. When the internal solitary wave propagates to the farthest measuring point, the wave height is only about half of that near the first measuring point. With the decrease of particle spacing, the numerical diffusion is greatly reduced. However, the wave height reduction caused by numerical diffusion is still obvious when the particle spacing of 0.002 m or 0.0015 m is adopted. As the particle spacing decreases to 0.001 m, the wave heights obtained at different

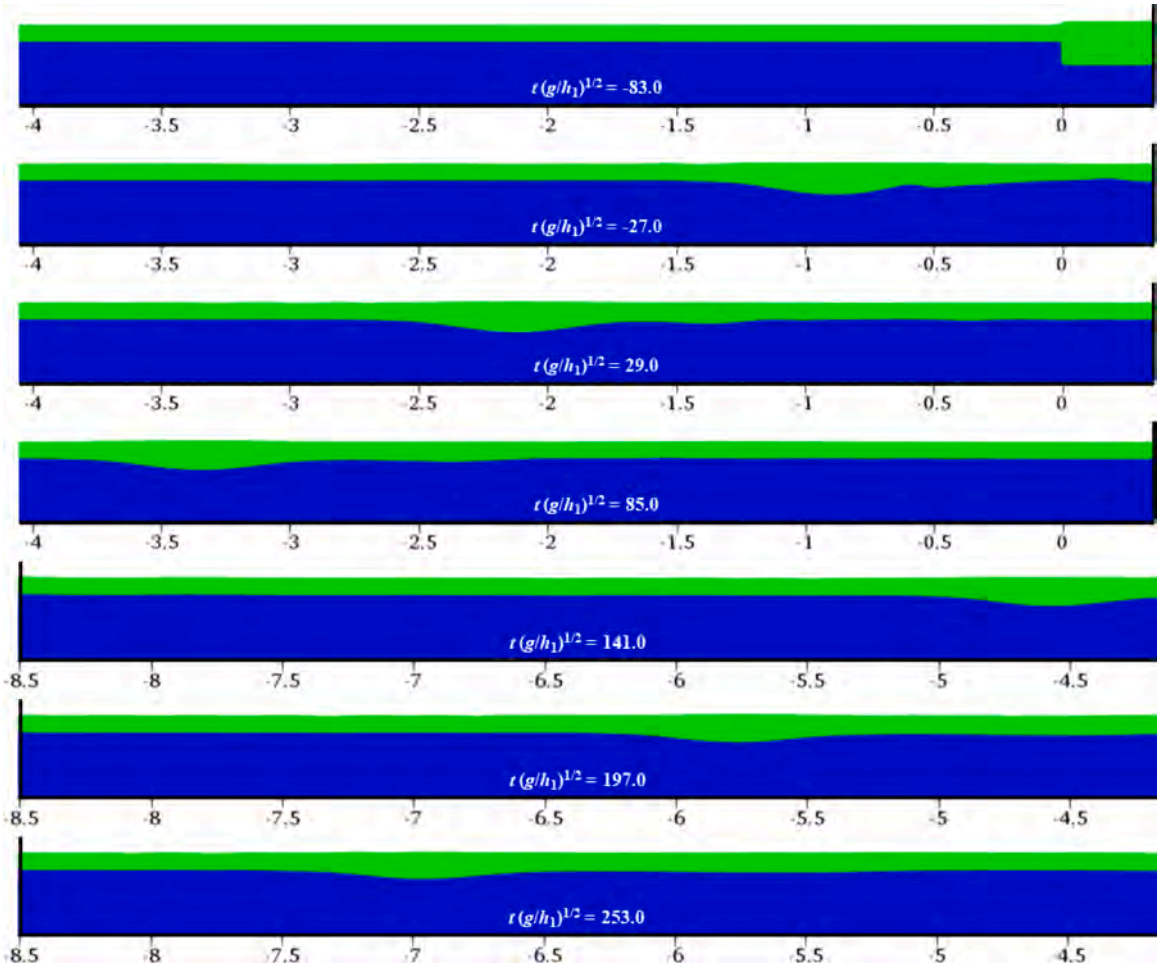

Fig. 43. Evolution of internal solitary wave, $dp = 0.001$ m, $h_3 = 0.09$ m.

measurement points become close, especially at the middle three measurement points, the wave heights keep almost consistent and the numerical diffusion can be ignored. Note that, the reason for the decrease of wave height between the first and second measuring points is that the wave profile has not being completely fixed. Due to the limitation of computing capacity, the smaller particle spacing is temporarily unable to be reached, but the calculation results still show a good convergence trend.

In Fig. 36, the wave heights calculated by multiphase MPS method with the initial particle spacing of 0.001 m are compared with the SPH (Zheng and Chen, 2019) and experimental (Kodaira et al., 2016) results. Both the MPS and SPH results are in good agreement with the experimental results, but the decrease of wave height for the MPS results is less. The reason may be that a large artificial viscosity is used in the SPH method to stabilize the calculation, which causes more numerical diffusion. In the MPS method, the real fluid viscosity can be directly adopted with the improvement of stability by the semi-implicit algorithm, thus the profiles of internal solitary wave can be better maintained even after a long-distance propagation, as shown in Fig. 37.

The pressure field during the stable propagation process is given in Fig. 38. Overall, the internal solitary wave imposes rather limited influence on the pressure field, which is close to the pressure field of static water. This also indicates that less wave energy is consumed to change the potential energy of the fluid system, thus the propagation distance of internal solitary wave can be much longer than the surface wave.

Fig. 39 shows the velocity field and the velocity vector distribution. It can be seen that the upper and lower fluids are induced to produce the opposite horizontal velocities and generate a violent shear flow, which is also one of the main sources of shear flows in the ocean. Meanwhile, the fluid moves downward in front of the trough and upward behind the trough, generating a vortex flow centered at the lowest point of the trough with an anticlockwise direction.

In order to further verify the accuracy of the present multiphase MPS method for the internal solitary waves with smaller amplitudes, the initial interfacial displacement h_3 is then reduced to 0.12 m and 0.09 m, respectively. Fig. 40 and Fig. 41 show the wave height and the evolution of internal solitary wave with $h_3 = 0.12$ m. With the decrease of the initial interfacial displacement, the wave height is significantly reduced compared with the case of $h_3 = 0.15$ m, and the waveform becomes relatively flatter. Notwithstanding this, the multiphase MPS results still show a good agreement with experimental results. The numerical results with $h_3 = 0.09$ m are presented in Fig. 42 and Fig. 43, from which a good agreement is observed again, even if the amplitude of internal solitary wave further decreases. Moreover, when the internal solitary wave propagates over a long distance and finally reaches the end of the numerical tank, the interface simulated by the multiphase MPS method is still clear and a regular waveform is maintained.

5. Conclusions

Based on the mesh-free MPS theory, this paper carried out two aspects of work, including the development of multiphase method and its application research on interfacial flows. Firstly, a multiphase MPS method with high accuracy and stability is developed from the improved moving particle semi-implicit (IMPS) method by introducing various multiphase models, and benefitting from the GPU acceleration

technique, the computational efficiency of multiphase MPS method is also enhanced, thus capable to large-scale 3-D simulations.

Then, the developed multiphase MPS method is widely applied to 2-D/3-D simulation of interfacial flows, including Rayleigh-Taylor instability, bubble rising, dam-break flow, and internal solitary waves, according to which the following conclusions can be drawn: (1) The fair agreements between the results of MPS and other reference results demonstrate that through the development of multiphase MPS method, the advantage of MPS method in free surface capturing can be further extended to track the complex interface in interfacial flows. (2) Although the air cavity formed in the dam-break flow is observed in both single-phase and multiphase simulations, only the multiphase MPS method is able to predict its profile and evolution exactly. Moreover, the multiphase MPS method is effective to correct the calculation error of pressure field caused by the neglection of air effect in the single-phase simulation.

Future work is necessary focusing on the further improvement of numerical schemes and computational efficiency of the multiphase MPS method. For example, the simulation of 3-D internal solitary waves is not performed in this paper, due to the requirement of a large number of particles and the huge computational cost. Besides, although the energy conservation of the present method has been verified by the simulation of internal solitary waves, more verifications are still needed for the stabilizing pressure gradient term as well as the multiphase collision model, such as the simulation of multi-fluid oscillating drop conducted by Khayyer et al. (2019). We also hope that the energy conservation property of the current multiphase MPS method can be further enhanced by introducing some higher-order or prominent numerical schemes, such as the HS, HL, ECS, DS and GC schemes (Khayyer et al., 2017b).

CRediT authorship contribution statement

Xiao Wen: Data curation, Writing – original draft, Visualization, Investigation, Software, Validation. **Weiwen Zhao:** Software, Data curation, Visualization, Investigation, Validation. **Decheng Wan:** Supervision, Conceptualization, Methodology, Investigation, Writing – review & editing.

Declaration of Competing Interest

None.

Acknowledgement

This work is supported by the National Key Research and Development Program of China (2019YFB1704200, 2019YFC0312401), National Natural Science Foundation of China (52131102, 51879159), to which the authors are most grateful.

References

Abbaszadeh, M., Alishahi, M.M., Emdad, H., 2020. Experimental investigations on the bubbly wake of a transom stern model using optical laser beam scattering characteristics. Appl. Ocean Res. 104, 102380.
Adelsberger, J., Esser, P., Griebel, M., Groß, S., Klitz, M., Rüttgers, A., 2014. 3D incompressible two-phase flow benchmark computations for rising droplets. In: Proceedings of the 11th World Congress on Computational Mechanics, WCCM XI, Barcelona, Spain, pp. 5274–5285.
Altomare, C., Gironella, X., Crespo, A.J.C., 2021. Simulation of random wave overtopping by a WCSPH model. Appl. Ocean Res. 116, 102888.
Bhat, N.U.H., Pahar, G., 2021. Euler-Lagrange framework for deformation of granular media coupled with the ambient fluid flow. Appl. Ocean Res. 116, 102857.
Brackbill, J.U., Kothe, D.B., Zemach, C., 1992. A continuum method for modeling surface tension. J. Comput. Phys. 100, 335–354.
Chen, X., Wan, D.C., 2019a. GPU accelerated MPS method for large-scale 3-D violent free surface flows. Ocean Eng 171, 677–694.
Chen, X., Wan, D.C., 2019b. Numerical simulation of three-dimensional violent free surface flows by GPU-based MPS method. Int. J. Comput. Methods 16 (4), 1–20.
Chen, X., Yao, X., Yang, N., Guo, K., Liu, L.T., 2019. Experimental investigation on the motion of bubbles in the moonpool with a sonar model inside. Appl. Ocean Res. 91, 101881.
Cheng, H., Ming, F.R., Sun, P.N., Sui, Y.T., Zhang, A.M., 2020. Ship hull slamming analysis with smoothed particle hydrodynamics method. Appl. Ocean Res. 101, 102268.
Chow, A.D., Rogers, B.D., Lind, S.J., Stansby, P.K., 2018. Incompressible SPH (ISPH) with fast poisson solver on a GPU. Comput. Phys. Commun. 226, 81–103.
Colagrossi, A., Landrini, M., 2003. Numerical simulation of interfacial flows by smoothed particle hydrodynamics. J. Comput. Phys. 191, 448–475.
Crespo, A.J.C., Gomez-Gesteira, M., Dalrymple, R.A., 2008. Modeling dam break behavior over a wet bed by a SPH technique. J. Waterway, Port, Coastal, Ocean Eng. 134, 313–320.
Crespo, A.J.C., Domínguez, J.M., Barreiro, A., Gomez-Gesteira, M., Rogers, B.D., 2011. GPUs, a new tool of acceleration in CFD: efficiency and reliability on smoothed particle hydrodynamics methods. PLoS ONE 6 (6), e20685.
Di Mascio, A., Marrone, S., Colagrossi, A., Chiron, L., Le Touzé, D., 2021. SPH-FV coupling algorithm for solving multi-scale three-dimensional free-surface flows. Appl. Ocean Res. 115, 102846.
Duan, G., Koshizuka, S., Chen, B., 2015. A contoured continuum surface force model for particle methods. J. Comput. Phys. 298, 280–304.
Duan, G., Koshizuka, S., Chen, B., Xiang, H., 2017. Stable multiphase moving particle semi-implicit method for incompressible interfacial flow. Comput. Methods Appl. Mech. Eng. 318, 636–666.
Gingold, R.A., Monaghan, J.J., 1977. Smoothed particle hydrodynamics: theory and application to non-spherical stars. Mon. Not. R. Astron. Soc. 191, 375–389.
Gotoh, H., Khayyer, A., Ikari, H., Arikawa, T., Shimosako, K., 2014. On enhancement of Incompressible SPH method for simulation of violent sloshing flows. Appl. Ocean Res. 46, 104–115.
Gotoh, H., Khayyer, A., 2016. Current achievements and future perspectives for projection-based particle methods with applications in ocean engineering. J. Ocean Eng. Mar. Energy 2, 1–28.
Gotoh, H., Khayyer, A., 2018. On the state-of-the-art of particle methods for coastal and ocean engineering. Coast. Eng. J. 60 (1), 79–103.
Gotoh, H., Khayyer, A., Shimizu, Y., 2021. Entirely lagrangian meshfree computational methods for hydroelastic fluid-structure interactions in ocean engineering—Reliability, adaptivity and generality. Appl. Ocean Res. 115, 102822.
Grisouard, N., Staquet, C., Gerkema, T., 2011. Generation of internal solitary waves in a pycnocline by an internal wave beam: a numerical study. J. Fluid Mech. 676, 491–513.
He, X., Zhang, R., Chen, S., Doolen, G.D., 1999. On the three-dimensional Rayleigh-Taylor instability. Phys. Fluids 11, 1143–1152.
Hori, C., Gotoh, H., Ikari, H., Khayyer, A., 2011. GPU-acceleration for moving particle semi-implicit method. Comput. Fluids 51, 174–183.
Hu, C., Sueyoshi, M., 2010. Numerical simulation and experiment on dam break problem. J. Marine. Sci. Appl. 9, 109–114.
Hysing, S., Turek, S., Kuzmin, D., Parolini, N., Burman, E., Ganesan, S., Tobiska, L., 2008. Quantitative benchmark computations of two-dimensional bubble dynamics. Int. J. Numer. Methods Fluids 60, 1259–1288.
Jandaghian, M., Shakibaeinia, A., 2020. An enhanced weakly-compressible MPS method for free-surface flows. Comput. Methods Appl. Mech. Eng. 360, 112771.
Ketabdari, M.J., Nobari, M.R.H., Moradi Larmaei, M., 2008. Simulation of waves group propagation and breaking in coastal zone using a Navier-Stokes solver with an improved VOF free surface treatment. Appl. Ocean Res. 30, 130–143.
Khayyer, A., Gotoh, H., 2008. Development of CMPS method for accurate water-surface tracking in breaking waves. Coast. Eng. J. 50 (2), 179–207.
Khayyer, A., Gotoh, H., 2009a. Modified moving particle semi-implicit methods for the prediction of 2D wave impact pressure. Coast. Eng. 56 (4), 419–440.
Khayyer, A., Gotoh, H., 2009b. Wave impact pressure calculations by improved SPH methods. Int. J. Offshore Polar 19 (04), 300–307.
Khayyer, A., Gotoh, H., Shao, S., 2009. Enhanced predictions of wave impact pressure by improved incompressible SPH methods. Appl. Ocean Res. 31 (2), 111–131.
Khayyer, A., Gotoh, H., 2010. A higher order Laplacian model for enhancement and stabilization of pressure calculation by the MPS method. Appl. Ocean Res. 32 (1), 124–131.
Khayyer, A., Gotoh, H., 2011. Enhancement of stability and accuracy of the moving particle semi-implicit method. J. Comput. Phys. 230 (8), 3093–3118.
Khayyer, A., Gotoh, H., 2016. A multiphase compressible-incompressible particle method for water slamming. Int. J. Offshore Polar 26, 20–25.
Khayyer, A., Gotoh, H., Shimizu, Y., 2017a. Comparative study on accuracy and conservation properties of two particle regularization schemes and proposal of an optimized particle shifting scheme in ISPH context. J. Comput. Phys. 332, 236–256.
Khayyer, A., Gotoh, H., Shimizu, Y., Gotoh, K., 2017b. On enhancement of energy conservation properties of projection-based particle methods. Eur. J. Mech. B-Fluid 66, 20–37.
Khayyer, A., Gotoh, H., Shimizu, Y., 2019. A projection-based particle method with optimized particle shifting for multiphase flows with large density ratios and discontinuous density fields. Comput. Fluids 179, 356–371.
Klaseboer, E., Hung, K.C., Wang, C., Wang, C.W., Khoo, B.C., Boyce, P., Debono, S., Charlier, H., 2005. Experimental and numerical investigation of the dynamics of an underwater explosion bubble near a resilient/rigid structure. J. Fluid Mech. 537, 387–413.
Kodaira, T., Waseda, T., Miyata, M., Choi, W., 2016. Internal solitary waves in a two-fluid system with a free surface. J. Fluid Mech. 804, 201–223.
Koshizuka, S., Oka, Y., 1996. Moving-particle semi-implicit method for fragmentation of incompressible fluid. Nuc. Sci. Eng. 123, 421–434.

Koshizuka, S., Nobe, A., Oka, Y., 1998. Numerical analysis of breaking waves using the moving particle semi-implicit method. Int. J. Numer. Methods Fluids 26, 751–769.
Lee, B.H., Park, J.C., Kim, M.H., Hwang, S.C., 2011. Step-by-step improvement of MPS method in simulating violent free-surface motions and impact-loads. Comput. Methods Appl. Mech. Eng. 200, 1113–1125.
Lee, H.G., Kim, J., 2013. Numerical simulation of the three-dimensional Rayleigh-Taylor instability. Comput. Math. Appl. 66, 1466–1474.
Lee, E.S., Moulinec, C., Xu, R., Violeau, D., Laurence, D., Stansby, P., 2008. Comparisons of weakly compressible and truly incompressible algorithms for the SPH mesh free particle method. J. Comput. Phys. 227, 8417–8436.
Li, X.L., Jin, B.X., Glimm, J., 1996. Numerical study for the three-dimensional Rayleigh-Taylor instability through the TVD/AC scheme and parallel computation. J. Comput. Phys. 126, 343–355.
Lobovský, L., Botia-Vera, E., Castellana, F., Mas-Soler, J., Souto-Iglesias, A., 2014. Experimental investigation of dynamic pressure loads during dam break. J. Fluids Strcut. 48, 407–434.
Lyu, W., Moctar, O., Potthoff, R., Neugebauer, J., 2017. Experimental and numerical investigation of sloshing using different free surface capturing methods. Appl. Ocean Res. 68, 307–324.
Lucy, L.B., 1977. A numerical approach to the testing of the fission hypothesis. Astron. J. 82, 1013–1024.
Luo, M., Khayyer, A., Lin, P., 2021. Particle methods in ocean and coastal engineering. Appl. Ocean Res. 114, 102734.
Marsooli, R., Wu, W., 2014. 3-D finite-volume model of dam-break flow over uneven beds based on VOF method. Adv. Water Resour. 70, 104–117.
Nomura, K., Koshizuka, S., Oka, Y., Obata, H., 2001. Numerical analysis of droplet breakup behavior using particle method. J. Nucl. Sci. Technol. 38 (12), 1057–1064.
Quartier, N., Crespo, A.J.C., Domínguez, J.M., Stratigaki, V., Troch, P., 2021. Efficient response of an onshore Oscillating Water Column Wave Energy Converter using a one-phase SPH model coupled with a multiphysics library. Appl. Ocean Res. 115, 102856.
Rao, C.P., Wan, D.C., 2018. Numerical study of the wave-induced slamming force on the elastic plate based on MPS-FEM coupled method. J. Hydrodyn. 30, 70–78.
Sampath, R., Zabaras, N., 2015. An object oriented implementation of a front tracking finite element method for directional solidification processes. Int. J. Numer. Meth. Eng. 44, 1227–1265.
Shakibaeinia, A., Jin, Y.C., 2010. A weakly compressible MPS method for modeling of open-boundary free-surface flow. Int. J. Numer. Meth. Fluids 63, 1208–1232.
Shakibaeinia, A., Jin, Y., 2012. MPS mesh-free particle method for multiphase flow. Comput. Methods Appl. Mech. Eng. 229-232, 13–26.
Shao, S., Lo, E.Y.M., 2003. Incompressible SPH method for simulating Newtonian and non-Newtonian flows with a free surface. Adv. Water Resour. 26, 787–800.
Shimizu, Y., Gotoh, H., Khayyer, A., 2018. An MPS-based particle method for simulation of multiphase flows characterized by high density ratios by incorporation of space potential particle concept. Comput. Math. Appl. 76, 1108–1129.
Tanaka, M., Masunaga, T., 2010. Stabilization and smoothing of pressure in MPS method by quasi-compressibility. J. Comput. Phys. 229, 4279–4290.
Tang, Z.Y., Wan, D.C., Chen, G., Xiao, Q., 2016a. Numerical simulation of 3D violent free-surface flows by multi-resolution MPS method. J. Ocean Eng. Mar. Energy 2, 355–364.
Tang, Z.Y., Zhang, Y.L., Wan, D.C., 2016b. Numerical simulation of 3-D free surface flows by overlapping MPS. J. Hydrodyn. 28, 306–312.
Wan, D.C., Shen, Z.R., Ma, Juan., 2010. Numerical simulations of viscous flows around surface ship by level set method. J. Hydrodyn. 22, 271–277.
Wang, Y., Qin, Y., Yao, X., 2020. A combined experimental and numerical investigation on damage characteristics of ice sheet subjected to underwater explosion load. Appl. Ocean Res. 103, 102347.
Xie, F.Z., Zhao, W.W., Wan, D.C., 2020. CFD simulations of three-dimensional violent sloshing flows in tanks based on MPS and GPU. J. Hydrodyn. 32 (4), 672–683.
Xie, F.Z., Zhao, W.W., Wan, D.C., 2021. Numerical simulations of liquid-solid flows with free surface by coupling IMPS and DEM. Appl. Ocean Res. 114, 102771.
Zhang, G., Wu, J., Sun, Z., Moctar, O., Zong, Z., 2020. Numerically simulated flooding of a freely-floating two-dimensional damaged ship section using an improved MPS method. Appl. Ocean Res. 101, 102207.
Zhang, G.Y., Zhao, W.W., Wan, D.C., 2021a. Partitioned MPS-FEM method for free-surface flows interacting with deformable structures. Appl. Ocean Res. 114, 102775.
Zhang, Z.L., Khalid, M.S.U., Long, T., Liu, M.B., Shu, C., 2021b. Improved element-particle coupling strategy with δ-SPH and particle shifting for modeling sloshing with rigid or deformable structures. Appl. Ocean Res. 114, 102774.
Zhang, X.S., Wang, J.H., Wan, D.C., 2021c. Euler-Lagrange study of bubble breakup and coalescence in a turbulent boundary layer for bubble drag reduction. Phys. Fluids 33, 037105.
Zhang, Y.L., Wan, D.C., 2017. Numerical study of interactions between waves and free rolling body by IMPS method. Comput. Fluids 155, 124–133.
Zhang, Y.X., Wan, D.C., 2011. Application of MPS in 3D dam breaking flows (in Chinese). Sci. Sin. Phys. Mech. Astron. 41, 140–154.
Zhang, Y.X., Wan, D.C., 2012. Apply MPS method to simulate liquid sloshing in LNG tank. In: Proceedings of the 22nd international offshore and polar engineering conference, pp. 381–391.
Zhao, X.D., Liang, S.X., Sun, Z.C., Zhao, X.Z., Sun, J.W., Liu, Z.B., 2017. A GPU accelerated finite volume coastal ocean model. J. Hydrodyn. 29 (4), 679–690.
Zheng, B.X., Chen, Z., 2019. A multiphase smoothed particle hydrodynamics model with lower numerical diffusion. J. Comput. Phys. 382, 177–201.
Zhou, Z.Q., De Kat, J.O., Buchner, B., 1999. A nonlinear 3D approach to simulate green water dynamics on deck. In: Proceedings of the Seventh International Conference on Numerical Ship Hydrodynamics, Nantes, France, pp. 1–15.
Zhu, X.S., Cheng, L., Lu, L., Teng, B., 2011. Implementation of the moving particle semi-implicit method on. GPU. Sci. China Phys. Mech. Astron. 54, 523–532.
Zou, L., Li, Y., Hu, Y., Wang, Z., Yu, Z., 2020. Frontal collision of two nonlinear internal solitary waves in a stratified fluid. Appl. Ocean Res. 104, 102334.